On the coupled thermo–electro–chemo–mechanical performance of structural batteries with emphasis on thermal effects

European Journal of Mechanics / A Solids 94 (2022) 104586

Contents lists available at ScienceDirect

European Journal of Mechanics / A Solids

journal homepage: www.elsevier.com/locate/ejmsol

On the coupled thermo–electro–chemo–mechanical performance of structural batteries with emphasis on thermal effects

David Carlstedt *, Kenneth Runesson, Fredrik Larsson, Leif E. Asp

Department of Industrial and Materials Science, Chalmers University of Technology, SE-412 96 Gothenburg, Sweden

ARTICLE INFO

Keywords:
Li-ion batteries
Multifunctional composites
Carbon fibre
Thermo–electro–chemo–mechanical coupling
Finite element analysis (FEA)

ABSTRACT

Carbon fibre (CF) based structural batteries is a type of battery designed to sustain mechanical loads. In this paper, a fully coupled thermo–electro–chemo–mechanical computational modelling framework for CF-based structural batteries is presented. We consider the combined effects of lithium insertion in the carbon fibres leading to insertion strains, and thermal expansion/shrinkage of the constituents leading to thermal (free) strains, while assuming transverse isotropy. The numerical studies show that the developed framework is able to capture the coupled thermo–electro–chemo–mechanical behaviour. Moreover, it is found that the dominating source for heat generation during galvanostatic cycling is associated with discontinuities in the electrical and chemical potentials at the fibre/electrolyte interface. Further, a limited parameter study shows that the temperature change during electrochemical cycling is significantly influenced by the applied current, thermal properties of the constituents and heat exchange with the surroundings. Finally, for large temperature variations, e.g. as identified during relevant (dis)charge conditions, the magnitude of the thermal strains in the structural battery electrolyte (SBE) are found to be similar to the insertion induced strains.

1. Introduction

Lithium-ion (Li-ion) batteries have been used for energy storage in electric vehicles and portable devices since the mid-'90s (Cano et al., 2018). However, the performance of conventional Li-ion batteries is limited by their energy storage to weight ratio (Cano et al., 2018; Armand et al., 2020). For example, to realize fully electric regional aircraft, this ratio needs to be increased compared with today's standard (Schäfer et al., 2019). A potential route to improve this ratio is to develop energy storage solutions with the ability to sustain mechanical loads (Asp et al., 2021; Federico et al., 2021; Moyer et al., 2020; Johannisson et al., 2018; Carlstedt and Asp, 2020; Yin et al., 2020; Wang et al., 2019; Lutkenhaus and Flouda, 2020; Asp et al., 2019; Ladpli et al., 2019). One such solution exploits electrodes consisting of carbon fibres (CFs) embedded in structural battery electrolyte (SBE). This type of material can be used in so-called "structural batteries", i.e. batteries with mechanical load-bearing capability (Asp et al., 2021; Moyer et al., 2020; Johannisson et al., 2018; Carlstedt and Asp, 2020; Yin et al., 2020) (see schematic illustration of the conceptual design of the laminated structural battery in Fig. 1a), in structural electrochemical actuators (Johannisson et al., 2020), or in structural energy harvesting and strain sensing materials (Jacques et al., 2013b; Harnden et al., 2022).

The SBE in the studied material is a bi-continuous bi-phasic composite which consists of two phases: (i) A solid phase, corresponding to a mechanically robust porous polymer network with an open pore system; (ii) A liquid phase which contains liquid electrolyte with Li-salt (cf. Ihrner et al. (2017) and Schneider et al. (2019)). The liquid phase in the porous polymer network enables ion transport between the electrodes, while the solid phase makes it possible to distribute mechanical loads. A schematic illustration of the SBE is presented in Fig. 1b, which corresponds to a numerically generated nano-structure, from Tu et al. (2020), representing an idealized fine-scale geometry of the SBE. The characteristic pore size of the polymer network is roughly in the order of 50–200 nm (Schneider et al., 2019). This can be compared with the typical diameter of a carbon fibre, which is approximately 5 μm.

It is well known that the electrochemical performance of conventional batteries is highly influenced by the temperature, see e.g. Al Hallaj et al. (1999), Thomas and Newman (2003) and Forgez et al. (2010). Moreover, the mechanical properties of conventional CF reinforced polymers (as construction material) are known to be highly affected by temperature (Gigliotti et al., 2011). Due to the fact that electrochemical cycling of a battery generates (or absorbs) heat, associated with e.g. transport of charge species and redox reactions, the

* Corresponding author.
E-mail address: david.carlstedt@chalmers.se (D. Carlstedt).

https://doi.org/10.1016/j.euromechsol.2022.104586
Received 30 November 2021; Received in revised form 10 February 2022; Accepted 15 March 2022
Available online 26 March 2022

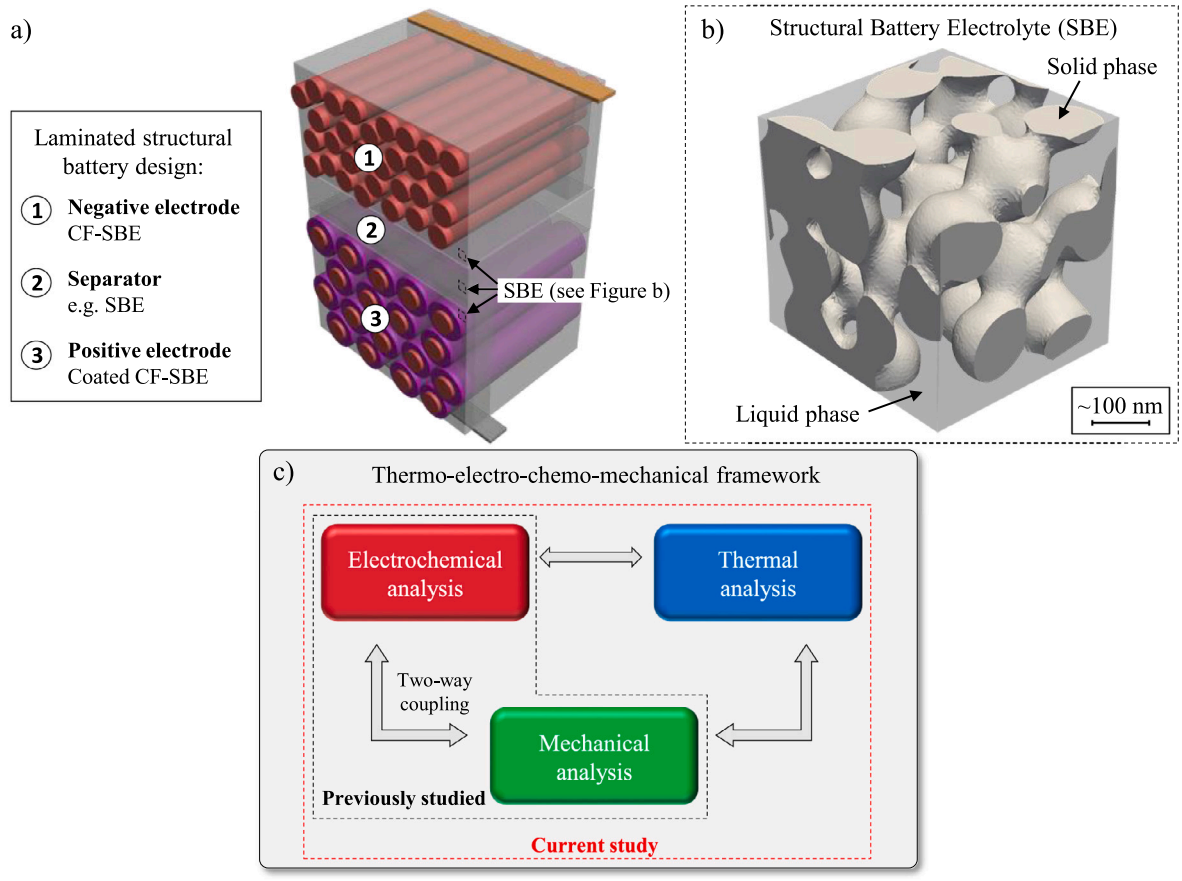

Fig. 1. (a) Schematic illustration of the conceptual design of the laminated structural battery. CF = Carbon fibre, SBE = Structural Battery Electrolyte. For information on coated-CF, see e.g. Hagberg et al. (2018) and Sanchez et al. (2021). (b) Numerically generated porous nano-structure, from Tu et al. (2020), representing an idealized fine-scale geometry of the SBE that consists of a polymer skeleton (solid phase) saturated with a liquid electrolyte phase. (c) Illustration of the developed thermo–electro–chemo–mechanical framework, and comparison with previous work (Carlstedt et al., 2020, 2022b,a).

temperature inside a battery will change during operation/service. This will alter the temperature dependent properties and induce thermal expansion/shrinkage of the constituents. Hence, it is crucial to be able to predict the distribution and evolution of temperature during operation as part of evaluating the multifunctional (i.e. coupled thermal, electrochemical and mechanical) performance of the structural battery material.

For conventional Li-ion batteries, a variety of approaches for modelling the thermo–electro–chemo–mechanical problem have been proposed, see e.g. Hu et al. (2017), Zhang et al. (2020), Duan et al. (2018) and Wang et al. (2021). However, only a few are developed based on a rigorous thermodynamics setting. In this context, we note an important contribution from Salvadori et al. (2018), who developed a fully coupled modelling framework for mass and heat transport, mechanics, and chemical reactions with trapping (which refers to the fact that only a fraction of the total available mass of mobile species is transported, whereas a significant counterpart remains immobile), based on non-equilibrium rational thermodynamics and small strain kinematics.

With respect to computational modelling of structural batteries, studies of various interactions between the electrochemical and mechanical fields have been carried out by the authors (Carlstedt et al., 2019) and by Xu et al. (2018a,b). Moreover, Tu et al. (2020) studied the bifunctional performance of the SBE on the nano-scale numerically. Goudarzi et al. (2022) have developed an efficient computational approach for modelling and simulation of electrochemical phenomena taking place in (three-dimensional) fibrous battery electrodes. Further, Pejman et al. (2021) developed a multi-physics design optimization framework for structural batteries and Yin et al. (2020) compared experimental and numerical results for modified CF electrodes in liquid electrolyte. In Yin et al. (2020), and in the accompanied work by Hong et al. (2021), the computational framework is based on the battery modelling scheme originally developed by Newman and co-workers (Newman and Tiedemann, 1975; Doyle et al., 1993; Newman and Thomas-Alyea, 2004) that presumes one-way coupling between the electrochemical and mechanical processes. Recently, the authors (Carlstedt et al., 2020) developed a thermodynamically consistent computational modelling framework to study the electro–chemo–mechanical properties of structural batteries while allowing for two-way coupling between the electrochemical and mechanical fields (Fig. 1c). In addition, the contribution to the ion transport from convection, i.e. from seepage of the liquid phase of the SBE, was accounted for in Carlstedt et al. (2022b), and numerical predictions were compared favourably with experimental data in Carlstedt et al. (2022a). However, in these studies isothermal conditions were assumed. With respect to the thermal interaction on the performance of structural batteries, only limited evaluation has been conducted. For example, Schutzeichel et al. (2019, 2021) studied, both experimentally and numerically, the thermal behaviour of multifunctional composite materials made from polymer electrolyte coated carbon fibres. Moreover, Carlstedt and Asp (Carlstedt and Asp, 2019) developed a semi-analytical framework to predict the mechanical consequences (thermal and diffusion induced stresses) from electrochemical cycling. In Carlstedt and Asp (2019), the electrochemical analysis was highly simplified and the analysis was limited to one-way coupling between the electrochemical and thermal analysis and the mechanical analysis. Hence, a complete modelling framework which accounts for the fully coupled thermal, electrochemical and mechanical processes in structural batteries is currently lacking.

In this paper we extend a previously developed (thermodynamically consistent) computational framework for structural batteries, Carlstedt et al. (2020), to account for thermal interaction effects (cf. Fig. 1c). The energy balance then becomes an additional governing equation, and the fully coupled thermo–electro–chemo–mechanical problem is solved for a simplified geometry with the appropriate constitutive relations and interface/boundary conditions. Numerical studies are performed to demonstrate the capability of the developed framework and to evaluate the effects of different coupling parameters. In particular, the significance of the individual terms linked to heat generation (or absorption) during galvanostatic (dis)charge conditions are evaluated, and a parameter study is carried out in order to assess the (additional) effect of the thermal properties on the combined thermal–electro–chemical–mechanical performance.

2. Studied half-cell and coupled analysis

To simplify the analysis we study the CF-SBE electrode half-cell illustrated in Fig. 2a. This simplification is motivated by the similarities of the two electrodes in the laminated structural battery architecture (both electrodes consist of fibres embedded in SBE), cf. Carlstedt et al. (2020, 2022b) and Fig. 1a. The basic design principle of the laminated structural battery is to create a laminate by stacking laminae with different functionalities. The design presented in Fig. 2a has the following laminae/components: (1) The working electrode, made from CFs embedded in SBE; (2) A separator layer, e.g. made from a thin layer of SBE; (3) The counter (and reference) electrode made from Li-metal.

The flow of charged species within the studied battery cell is schematically illustrated in Fig. C.10a–b in Appendix C. We note that the electrons in the fibres are assumed to flow in the fibre direction only. Further, we assume a linear distribution of the electronic current along the fibre (illustrated in Fig. C.10c). This leads to the idealized conditions where the current input is the same at all cross-sections along the fibre direction, which allows us to simplify the analysis and only study one cross-section (2D-analysis). Moreover, the electron flow in the Li-metal as well as the current collections, (electron) conductive adhesive and external circuit are neglected (for simplicity).

The idealized material representation of the studied half-cell is presented in Fig. 2b and corresponds to a repeatable unit in the x_1-direction of the CF-SBE electrode lamina. It should be noted that the separator is excluded (for the sake of simplicity) but can easily be added as an additional electrolyte phase, as e.g. done is Carlstedt et al. (2022a). Moreover, we note that the SBE is treated as a continuum at the studied length-scale and effective properties are utilized (cf. Carlstedt et al. (2022b)). The introduced notation is defined in Section 3.

Finally, a schematic illustration of the coupled thermo–electro–chemo–mechanical problem is presented in Fig. 2c. The pertinent balance equations are linear momentum balance, charge balance (Gauss law), mass balance, and energy balance. The basic independent fields are the displacement field $\boldsymbol{u}$, the electrical potential φ, the ion concentrations c_α and chemical potentials μ_α of species α =Li,X, and the (absolute) temperature θ.

3. Time-continuous strong format and modelling assumptions

The time-continuous strong format and modelling assumptions for the individual domains, interfaces and boundaries are presented in this section. We thereby extend the theory, as compared with previous work by the authors (Carlstedt et al., 2020), to account for thermal effects associated with the electrochemical and mechanical processes. Moreover, a detailed derivation of the thermodynamics for a generic electro–chemical–thermal–mechanical system (not necessarily the actual battery) is presented in Appendix A.

3.1. Fibre domain(s)

The fibre domain(s) are denoted $\Omega_\mathrm{f} = \cup_i^{N_\mathrm{fibres}} \Omega_{\mathrm{f},i}$ (cf. Fig. 2b). The following special assumptions are introduced: (i) Material properties are characterized as transversely isotropic (isotropy pertains to the cross-section, defined by Cartesian coordinates x_1, x_2); (ii) The single active species is Li, which moves into (and out from) the fibre; (iii) The fibres (Ω_f) and the positive connector (Γ_+) are connected via an external circuit. It is assumed that the electric potential is uniform (and equal) in all fibres, $\varphi(\boldsymbol{x}, t) = \Phi^-(t)$, for $\boldsymbol{x} \in \Omega_\mathrm{f} = \cup_i^{N_\mathrm{fibres}} \Omega_{\mathrm{f},i}$; consequently, the electric field is zero within the fibre domain. Although the analysis is two-dimensional (restricted to the x_1, x_2-plane), so-called resistive (Joule) heat generation along the fibres is accounted for in an approximate fashion.

3.1.1. Balance equations

The governing balance equations in the fibre domain(s) (Ω_f) are expressed in the strong format as follows:

$$-\boldsymbol{\sigma} \cdot \boldsymbol{\nabla} = \boldsymbol{0} \text{ in } \Omega_\mathrm{f} \times \mathbb{R}^+ \tag{1a}$$

$$\rho \partial_t c_\mathrm{Li} + \boldsymbol{j}_\mathrm{Li} \cdot \boldsymbol{\nabla} = 0 \text{ in } \Omega_\mathrm{f} \times \mathbb{R}^+ \tag{1b}$$

$$C_\mathrm{v} \partial_t \theta + \boldsymbol{q} \cdot \boldsymbol{\nabla} + \boldsymbol{j}_\mathrm{Li} \cdot \boldsymbol{\nabla} \mu_\mathrm{Li} = Q_\mathrm{elec} \text{ in } \Omega_\mathrm{f} \times \mathbb{R}^+ \tag{1c}$$

where $\boldsymbol{\sigma}$ is the (symmetric) stress tensor, $\boldsymbol{j}_\mathrm{Li}$ is the ion flux vector for Li, $\boldsymbol{q}$ is the heat flux vector, c_Li is the ion concentration of Li,[1] μ_Li is the chemical potential of Li, and θ is the (absolute) temperature. The generated heat due to the electric current in the fibre is denoted Q_elec (see Section 3.1.3). Moreover, ρ is the bulk density and C_v is the volume-specific heat capacity.

Remark 1. The contributions to the energy balance with respect to $\boldsymbol{\sigma}$ and μ_Li, denoted $\boldsymbol{\beta}$ and γ_Li, are derivable theoretically in a thermodynamically consistent fashion, cf. Appendix A. However, we have simplified the energy equation from the outset by setting $\boldsymbol{\beta} = \boldsymbol{0}$ and $\gamma_\mathrm{Li} = 0$. To ignore $\boldsymbol{\beta}$ is standard for quasi-static mechanical loading. Further, γ_Li is often neglected in the battery modelling literature (see e.g. Hu et al. (2017)).

3.1.2. Constitutive relations

In order to obtain explicit expressions of the purely energetic quantities $\boldsymbol{\sigma}$ and μ_Li, we introduce the following partial free energy densities

$$\psi^{\text{me-th-ch}}(\boldsymbol{\epsilon}, \theta, c_\mathrm{Li}) = \frac{1}{2} \left[\boldsymbol{\epsilon} - \boldsymbol{\epsilon}^\mathrm{ch}(c_\mathrm{Li}) - \boldsymbol{\epsilon}^\mathrm{th}(\theta)\right] : \mathbf{E}(c_\mathrm{Li}) : \left[\boldsymbol{\epsilon} - \boldsymbol{\epsilon}^\mathrm{ch}(c_\mathrm{Li}) - \boldsymbol{\epsilon}^\mathrm{th}(\theta)\right] \tag{2a}$$

$$\psi_\mathrm{Li}^\mathrm{ch}(\theta, c_\mathrm{Li}) = \rho \left[c_\mathrm{Li} \left[\mu_\mathrm{Li}^0 - R\theta_0 \log\left(\frac{\tilde{c}'_{\mathrm{Li},0}}{1 - \tilde{c}'_{\mathrm{Li},0}} \right) \right] + R\theta \int_{c_{\mathrm{Li},0}}^{c_\mathrm{Li}} \log\left(\frac{\tilde{c}'_\mathrm{Li}}{1 - \tilde{c}'_\mathrm{Li}} \right) \mathrm{d}c'_\mathrm{Li} \right] \tag{2b}$$

$$\psi^\mathrm{th}(\theta) = -\frac{1}{2\theta_0} C_\mathrm{v} \left[\theta - \theta_0\right]^2 \tag{2c}$$

where μ_Li^0 is a reference/standard value of the chemical potential and R is the universal gas constant. As to the introduced variables, $\boldsymbol{\epsilon}[\boldsymbol{u}]$ is the (small) strain tensor expressed as a linear operator of the displacement field $\boldsymbol{u}$, and $\tilde{c}_\mathrm{Li} := \frac{c_\mathrm{Li}}{c_{\mathrm{Li,max}}}$ is the normalized mass concentration of Li (with respect to the assumed maximum Li-concentration $c_{\mathrm{Li,max}}$). It should be noted that we have assumed that the specific heat (C_v) and the elastic tensor ($\mathbf{E}$) are temperature independent (for simplicity). Further, Eq. (2b) is expressed such that the reference state for the

[1] It should be noted that c_Li is defined in mol kg^{-1}, and not in mol m^{-3} commonly used in the electrochemistry literature (cf. Newman and Thomas-Alyea (2004)).

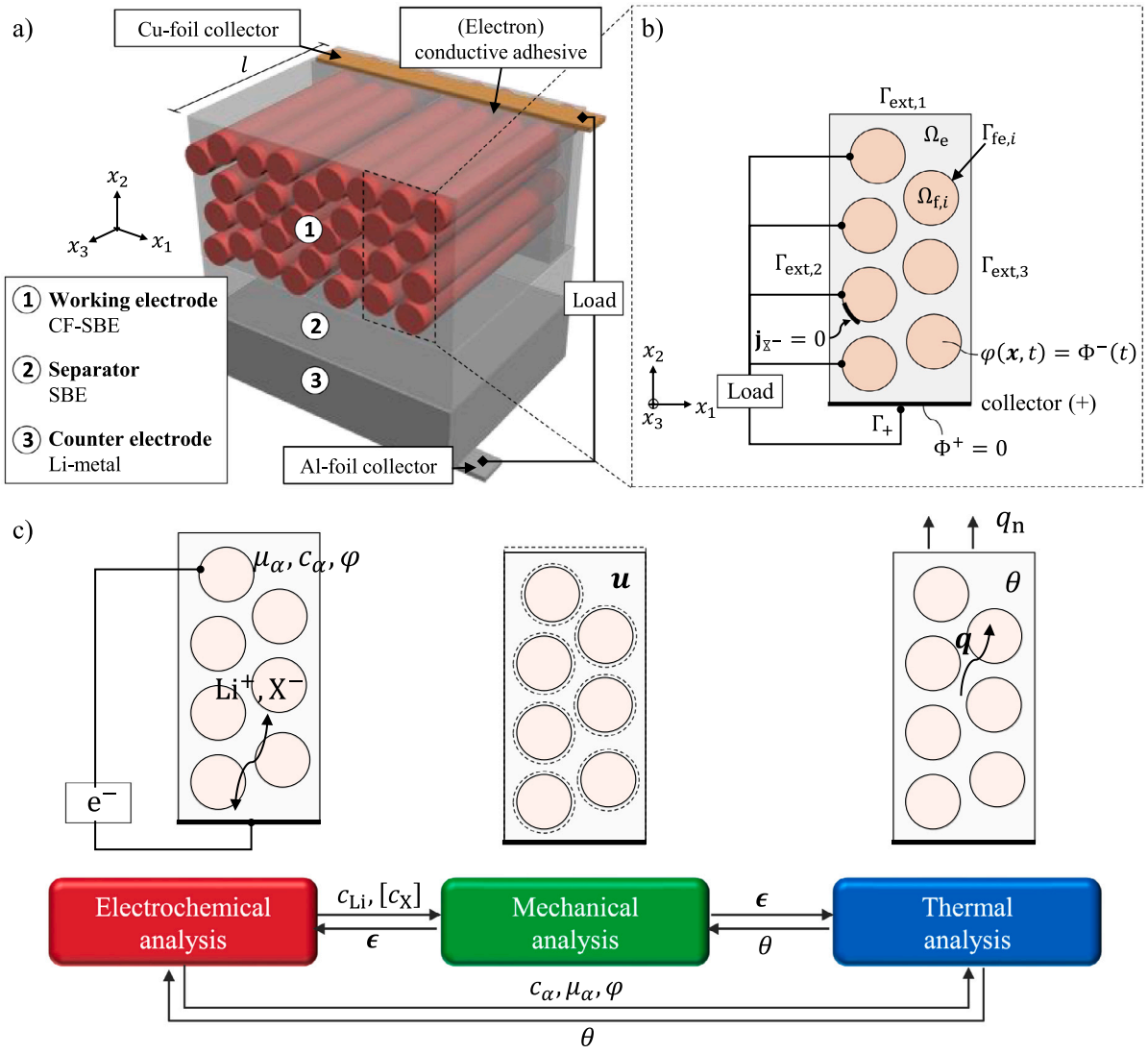

Fig. 2. (a) Conceptual design of the studied CF-SBE electrode half-cell. (b) Schematic architecture (generic/idealized model representation) of the studied half-cell. In the external circuit, Load represents electric loading. (c) A schematic illustration of the coupled thermo–electro–chemo–mechanical problem. The introduced notation is defined in Section 3.

chemical potential is defined at $\boldsymbol{u} = \boldsymbol{0}$, $c_{\mathrm{Li}} = c_{\mathrm{Li},0}$ and $\theta = \theta_0$. Moreover, ϵ^{ch} and ϵ^{th} are the insertion and thermal (free) strains, defined as

$$\epsilon^{\mathrm{ch}}(c_{\mathrm{Li}}) = \boldsymbol{\alpha}^{\mathrm{ch}}\left[c_{\mathrm{Li}} - c_{\mathrm{Li},0}\right] \tag{3a}$$

$$\epsilon^{\mathrm{th}}(\theta) = \boldsymbol{\alpha}^{\mathrm{th}}\left[\theta - \theta_0\right] \tag{3b}$$

where the reference/initial values $c_{\mathrm{Li},0}$ and θ_0 denote the state of a pristine material, i.e. the state at which no chemical or thermal strains are present in the material, respectively. Further, $\boldsymbol{\alpha}^{\mathrm{ch}}$ and $\boldsymbol{\alpha}^{\mathrm{th}}$ are second order tensors containing the coefficients of the lithium insertion and thermal induced expansion of the fibres, respectively, and they are defined as[2]

$$\boldsymbol{\alpha}^{\mathrm{ch}} = \alpha_{\perp}^{\mathrm{ch}}\left[\boldsymbol{E}_1 + \boldsymbol{E}_2\right] + \alpha_{\parallel}^{\mathrm{ch}}\boldsymbol{E}_3 \tag{4a}$$

$$\boldsymbol{\alpha}^{\mathrm{th}} = \alpha_{\perp}^{\mathrm{th}}\left[\boldsymbol{E}_1 + \boldsymbol{E}_2\right] + \alpha_{\parallel}^{\mathrm{th}}\boldsymbol{E}_3 \tag{4b}$$

where $\alpha_{\perp}^{\mathrm{ch}}$, $\alpha_{\perp}^{\mathrm{th}}$ and $\alpha_{\parallel}^{\mathrm{ch}}$, $\alpha_{\parallel}^{\mathrm{th}}$ are the transverse and longitudinal expansions coefficients associated with lithium insertion and thermal expansion, respectively. Finally, as to the elasticity tensor that is pertinent to transverse isotropy, it is defined by five independent parameters as follows:

$$\begin{aligned}\mathbf{E}(c_{\mathrm{Li}}) = \; & L_{\perp}(c_{\mathrm{Li}})\boldsymbol{I}\otimes\boldsymbol{I} + 2G_{\perp}\mathbf{I}^{\mathrm{sym}} + [L_{\parallel} - L_{\perp}(c_{\mathrm{Li}})][\boldsymbol{I}\otimes\boldsymbol{E}_3 + \boldsymbol{E}_3\otimes\boldsymbol{I}] \\ & + [H_{\parallel} - 4G_{\parallel} + 2G_{\perp} - 2L_{\parallel} + L_{\perp}(c_{\mathrm{Li}})]\boldsymbol{E}_3\otimes\boldsymbol{E}_3 + 4[G_{\parallel} - G_{\perp}]\mathbf{A}\end{aligned} \tag{5}$$

where $\boldsymbol{I} = \boldsymbol{E}_1 + \boldsymbol{E}_2 + \boldsymbol{E}_3$ is the 2nd order identity tensor, $\mathbf{I}^{\mathrm{sym}} := \frac{1}{2}[\boldsymbol{I}\overline{\otimes}\boldsymbol{I} + \boldsymbol{I}\underline{\otimes}\boldsymbol{I}]$ is the (symmetric) 4th order identity tensor,[3] whereas $\mathbf{A} := \frac{1}{4}[\boldsymbol{E}_3\overline{\otimes}\boldsymbol{I} + \boldsymbol{E}_3\underline{\otimes}\boldsymbol{I} + \boldsymbol{I}\overline{\otimes}\boldsymbol{E}_3 + \boldsymbol{I}\underline{\otimes}\boldsymbol{E}_3]$ is a 4th order symmetric tensor. Lamé's first parameter is denoted L, the shear modulus is denoted G, whereas $H_{\parallel}$ is the uniaxial strain modulus. Since measurements have shown that it is mainly the transverse elastic modulus of the carbon fibre that is significantly influenced by lithiation (Duan et al., 2021), $L_{\perp}(c_{\mathrm{Li}})$ is the only elastic modulus that is chosen to depend on the Li-concentration.

We are now in the position to compute

$$\boldsymbol{\sigma} = \boldsymbol{\sigma}^{\mathrm{en}}(\boldsymbol{\epsilon}, c_{\mathrm{Li}}, \theta) := \mathbf{E}(c_{\mathrm{Li}}) : \left[\boldsymbol{\epsilon}[\boldsymbol{u}] - \boldsymbol{\epsilon}^{\mathrm{ch}}(c_{\mathrm{Li}}) - \boldsymbol{\epsilon}^{\mathrm{th}}(\theta)\right] \tag{6a}$$

$$\mu_{\mathrm{Li}} = \mu_{\mathrm{Li}}^{\mathrm{en}}(\boldsymbol{\epsilon}, c_{\mathrm{Li}}, \theta) := \mu_{\mathrm{Li}}^{0} - R\theta_0 \log\left(\frac{\tilde{c}_{\mathrm{Li},0}}{1-\tilde{c}_{\mathrm{Li},0}}\right) + R\theta \log\left(\frac{\tilde{c}_{\mathrm{Li}}}{1-\tilde{c}_{\mathrm{Li}}}\right)$$

[2] $\boldsymbol{E}_i := \boldsymbol{e}_i \otimes \boldsymbol{e}_i$ is the i:th base dyad.

[3] Indicial notation: $(\boldsymbol{A}\overline{\otimes}\boldsymbol{B})_{ijkl} \overset{\mathrm{def}}{=} (\boldsymbol{A})_{ik}(\boldsymbol{B})_{jl}$, $(\boldsymbol{A}\underline{\otimes}\boldsymbol{B})_{ijkl} \overset{\mathrm{def}}{=} (\boldsymbol{A})_{il}(\boldsymbol{B})_{jk}$ for $\boldsymbol{A}$, $\boldsymbol{B}$ symmetric 2nd order tensors.

$$- \rho^{-1}\boldsymbol{\alpha}^{\mathrm{ch}} : \boldsymbol{\sigma}(\boldsymbol{\epsilon}, c_{\mathrm{Li}}, \theta) + \rho^{-1}\frac{1}{2}[\boldsymbol{\epsilon} - \boldsymbol{\epsilon}^{\mathrm{ch}}(c_{\mathrm{Li}}) - \boldsymbol{\epsilon}^{\mathrm{th}}(\theta)] : \frac{\partial \mathbf{E}(c_{\mathrm{Li}})}{\partial c_{\mathrm{Li}}} : [\boldsymbol{\epsilon} - \boldsymbol{\epsilon}^{\mathrm{ch}}(c_{\mathrm{Li}}) - \boldsymbol{\epsilon}^{\mathrm{th}}(\theta)] \tag{6b}$$

It appears that the initial values of $\boldsymbol{\sigma}$ and μ_{Li} are $\boldsymbol{\sigma}^{\mathrm{en}}(\mathbf{0}, c_{\mathrm{Li},0}, \theta_0) = \mathbf{0}$ and $\mu_{\mathrm{Li}}^{\mathrm{en}}(\mathbf{0}, c_{\mathrm{Li},0}, \theta_0) = \mu_{\mathrm{Li}}^0$.

Next, we consider the "dissipative" variables $\boldsymbol{j}_{\mathrm{Li}}$ and $\boldsymbol{q}$, whose constitutive relations are chosen as

$$\boldsymbol{j}_{\mathrm{Li}}(c_{\mathrm{Li}}) = -\boldsymbol{M}_{\mathrm{Li}}(c_{\mathrm{Li}}) \cdot \boldsymbol{\nabla}\mu_{\mathrm{Li}} \tag{7a}$$

$$\boldsymbol{q}(\theta) = -\boldsymbol{K} \cdot \boldsymbol{\nabla}\theta \tag{7b}$$

where we introduced the mobility tensor and thermal conductivity tensor as follows:

$$\boldsymbol{M}_{\mathrm{Li}}(c_{\mathrm{Li}}) = \eta_{\mathrm{Li},\perp}\rho c_{\mathrm{Li}}\left[\boldsymbol{E}_1 + \boldsymbol{E}_2\right] + \eta_{\mathrm{Li},\parallel}\rho c_{\mathrm{Li}}\boldsymbol{E}_3 \tag{8a}$$

$$\boldsymbol{K} = k_{\perp}\left[\boldsymbol{E}_1 + \boldsymbol{E}_2\right] + k_{\parallel}\boldsymbol{E}_3 \tag{8b}$$

The mobilities in the transverse and longitudinal directions are denoted $\eta_{\mathrm{Li},\perp}$ and $\eta_{\mathrm{Li},\parallel}$, respectively. Similarly, the thermal conductivity coefficients in the transverse and longitudinal directions are denoted $k_{\perp}$ and $k_{\parallel}$, respectively.

Remark 2. The dissipative variables $\boldsymbol{j}_{\mathrm{Li}}$ and $\boldsymbol{q}$ (cf. Eqs. (7a)–(7b)) are motivated by dissipation inequality (see Appendices A.3.2 and A.3.3 in Appendix A).

3.1.3. Generated heat in the carbon fibre

The (only) source term of heat supply in Eq. (1c), denoted Q_{elec}, stems from the power that is dissipated due to electric current along the fibres, whereby we recall that the fibres work as both electrodes for the ionic transport (diffusion) as well as current collectors. The question is how to compute this term in a two-dimensional analysis? In a proper three-dimensional analysis the situation is more obvious, since the effect of any current $\boldsymbol{i}$ in the energy equation can be written as $Q_{\mathrm{elec}} = \boldsymbol{i}_{\mathrm{e}}^{-} \cdot \boldsymbol{e}$, cf. Eq. (A.20), where $\boldsymbol{i}_{\mathrm{e}}^{-}$ is the (part of the) current that is due to electronic transport. To motivate the proper expression of Q_{elec} in the present two-dimensional analysis, we thus argue as follows:

First, we recall the assumption that the electric potential is constant ($\varphi = \Phi^{-}$) within each fibre cross-section, collectively occupying the domain Ω_{f}. This means that there is no electric current in the cross-sectional plane. However, in reality φ must vary along the fibres, giving rise to an electric field component $e^{\mathrm{f}} := (\boldsymbol{e})_3 = -\frac{\partial \varphi}{\partial x_3}$ and, thus, a resulting current $i^{\mathrm{f}} := (\boldsymbol{i}_{\mathrm{e}}^{-})_3$. Further, we assume that the constitutive equation for i^{f} is $i^{\mathrm{f}} = \kappa^{\mathrm{f}} e^{\mathrm{f}}$, where κ^{f} is a (constant) electric conductivity. Hence, we obtain the simple expression

$$Q_{\mathrm{elec}} = i^{\mathrm{f}} e^{\mathrm{f}} = \kappa^{\mathrm{f}}[e^{\mathrm{f}}]^2 = [\kappa^{\mathrm{f}}]^{-1}[i^{\mathrm{f}}]^2 \tag{9}$$

It only remains to determine the value of either e^{f} or i^{f}. In the particular case of galvanostatic control with a prescribed supplied current I^{-} via the fibre perimeter per unit length of the fibre [A/m] (which is the case studied in this paper), we assume that i^{f} is equal in each fibre and that the current varies linearly along the fibres. Further, we approximate the generated heat at the evaluated cross-section as the average value of the total Q_{elec} (with respect to the total fibre length l). This corresponds to assuming an average current of

$$i_{\mathrm{ave}}^{\mathrm{f}} = \frac{I^{-} l}{\sqrt{3} A^{\mathrm{f}}} \tag{10}$$

where A^{f} is the total cross-sectional area of all fibres and l is the fibre length (cf. Fig. 2a). This gives the approximated expression

$$Q_{\mathrm{elec}} = \frac{[I^{-}]^2 l^2}{3[A^{\mathrm{f}}]^2 \kappa^{\mathrm{f}}} \tag{11}$$

We note that the total current extracted from the cell then becomes $I^{-} l$. In a potentiostatic problem on the other hand, the value I^{-} is part of the solution, i.e. Eq. (11) has to be evaluated as part of the problem formulation. It should be noted that we assume a finite electric conductivity of the fibres when estimating the generated heat in the fibres, while we assume a constant electric potential along the fibre (as discussed in Section 2) for the cross-sectional problem. We note that this is not consistent with the energy conservation of the system. However, this assumption is made to simplify the analysis in order to allow for utilizing a 2D-model representation while estimating the temperature increase during operation. Without this assumption, the potential at the fibre would be different at different cross-sections.

3.2. Electrolyte (or SBE) domain

The electrolyte (or SBE) domain is denoted Ω_{e} (cf. Fig. 2b). The following special assumptions are introduced: (i) Material properties are characterized as isotropic; (ii) The Li-ions are positively charged (cation) and the companion X-ions (anion) are negatively charged; (iii) The current density is carried both by Li^{+} and the companion anion X^{-}.

3.2.1. Balance equations

The governing balance equations in the electrolyte domain (Ω_{e}) are expressed in the strong format as follows:

$$-\boldsymbol{\sigma} \cdot \boldsymbol{\nabla} = \mathbf{0} \text{ in } \Omega_{\mathrm{e}} \times \mathbb{R}^{+} \tag{12a}$$

$$-\rho^{\mathrm{F}} F[c_{\mathrm{Li}} - c_{\mathrm{X}}] + \boldsymbol{d} \cdot \boldsymbol{\nabla} = 0 \text{ in } \Omega_{\mathrm{e}} \times \mathbb{R}^{+} \tag{12b}$$

$$\rho^{\mathrm{F}}\partial_t c_{\mathrm{Li}} + \boldsymbol{j}_{\mathrm{Li}} \cdot \boldsymbol{\nabla} = 0 \text{ in } \Omega_{\mathrm{e}} \times \mathbb{R}^{+} \tag{12c}$$

$$\rho^{\mathrm{F}}\partial_t c_{\mathrm{X}} + \boldsymbol{j}_{\mathrm{X}} \cdot \boldsymbol{\nabla} = 0 \text{ in } \Omega_{\mathrm{e}} \times \mathbb{R}^{+} \tag{12d}$$

$$C_{\mathrm{v}}\partial_t \theta + \boldsymbol{q} \cdot \boldsymbol{\nabla} + \boldsymbol{j}_{\mathrm{Li}} \cdot \boldsymbol{\nabla}\mu_{\mathrm{Li}} + \boldsymbol{j}_{\mathrm{X}} \cdot \boldsymbol{\nabla}\mu_{\mathrm{X}} + F[\boldsymbol{j}_{\mathrm{Li}} - \boldsymbol{j}_{\mathrm{X}}] \cdot \boldsymbol{\nabla}\varphi = 0 \text{ in } \Omega_{\mathrm{e}} \times \mathbb{R}^{+} \tag{12e}$$

In addition to those variables already introduced for the fibre domain, we introduced the following notation: $\boldsymbol{d}$ is the electric flux density vector (dielectric displacement), c_{Li} and c_{X} are the ion concentrations of Li and X, respectively (defined as ion mass, in moles, per unit mass of fluid, in kg). Moreover, μ_{X} is the chemical potential and $\boldsymbol{j}_{\mathrm{X}}$ is the ion flux vector for the species X. Finally, ρ^{F} is the intrinsic density of the fluid (electrolyte) in the SBE and F is Faraday's constant.

Remark 3. In analogy with the situation for the fibres, we have simplified the energy equation from the outset by setting $\boldsymbol{\beta} = \mathbf{0}$, $\gamma_{\mathrm{Li}} = 0$ and $\gamma_{\mathrm{X}} = 0$, cf. Appendix A.

3.2.2. Constitutive relations

In order to obtain explicit expressions of the purely energetic quantities $\boldsymbol{\sigma}$, $\boldsymbol{d}$, μ_{Li}, and μ_{X}, we introduce the following partial free energy densities

$$\psi^{\text{me-th-ch}}(\boldsymbol{\epsilon}, \theta) = \frac{1}{2}\left[\boldsymbol{\epsilon} - \boldsymbol{\epsilon}^{\mathrm{th}}(\theta)\right] : \mathbf{E} : \left[\boldsymbol{\epsilon} - \boldsymbol{\epsilon}^{\mathrm{th}}(\theta)\right] \tag{13a}$$

$$\psi^{\mathrm{el}}(\boldsymbol{e}) = -\frac{1}{2}\boldsymbol{e} \cdot \boldsymbol{\mathcal{E}} \cdot \boldsymbol{e} \tag{13b}$$

$$\psi_{\mathrm{Li}}^{\mathrm{ch}}(\theta, c_{\mathrm{Li}}) = \rho^{\mathrm{F}}\left[c_{\mathrm{Li}}\left[\mu_{\mathrm{Li}}^0 - R\theta_0 \log\left(\tilde{c}'_{\mathrm{Li},0}\right)\right] + R\theta\int_{c_{\mathrm{Li},0}}^{c_{\mathrm{Li}}} \log\left(\tilde{c}'_{\mathrm{Li}}\right)\, \mathrm{d}c'_{\mathrm{Li}}\right] \tag{13c}$$

$$\psi_{\mathrm{X}}^{\mathrm{ch}}(\theta, c_{\mathrm{X}}) = \rho^{\mathrm{F}}\left[c_{\mathrm{X}}\left[\mu_{\mathrm{X}}^0 - R\theta_0 \log\left(\tilde{c}'_{\mathrm{X},0}\right)\right] + R\theta\int_{c_{\mathrm{X},0}}^{c_{\mathrm{X}}} \log\left(\tilde{c}'_{\mathrm{X}}\right)\, \mathrm{d}c'_{\mathrm{X}}\right] \tag{13d}$$

$$\psi^{\mathrm{th}}(\theta) = -\frac{1}{2\theta_0}C_{\mathrm{v}}\left[\theta - \theta_0\right]^2 \tag{13e}$$

where $\boldsymbol{e} := -\boldsymbol{\nabla}\varphi$ is the electric field.[4] The only free strain in the electrolyte is the thermal induced strain, which is given as

$$\boldsymbol{\epsilon}^{\mathrm{th}}(\theta) = \boldsymbol{\alpha}^{\mathrm{th}}\left[\theta - \theta_0\right] \tag{14}$$

where $\boldsymbol{\alpha}^{\mathrm{th}} := \alpha^{\mathrm{th}}\boldsymbol{I}$ is the isotropic thermal expansion tensor. The standard isotropic elasticity tensor is expressed in terms of Lamé's parameters as

$$\mathbf{E} = L\boldsymbol{I}\otimes\boldsymbol{I} + 2G\mathbf{I}^{\mathrm{sym}} \tag{15}$$

where L is Lamé's first parameter and G is the shear modulus. Moreover, the isotropic permittivity tensor is given as:

$$\boldsymbol{\mathcal{E}} = \varepsilon_0\varepsilon_r\boldsymbol{I} \tag{16}$$

where ε_0 and ε_r are the vacuum and relative permittivity, respectively. In analogy with the situation for the fibre domain, we define the normalized ion concentration of species Li and X as $\tilde{c}_{\mathrm{Li}} = \frac{c_{\mathrm{Li}}}{c_{\mathrm{Li,ref}}}$ and $\tilde{c}_{\mathrm{X}} = \frac{c_{\mathrm{X}}}{c_{\mathrm{X,ref}}}$, respectively.[5]

We are now in the position to compute

$$\boldsymbol{\sigma} = \boldsymbol{\sigma}^{\mathrm{en}}(\boldsymbol{\epsilon},\theta) := \mathbf{E} : \left[\boldsymbol{\epsilon}[\boldsymbol{u}] - \boldsymbol{\epsilon}^{\mathrm{th}}(\theta)\right] \tag{17a}$$

$$\boldsymbol{d} = \boldsymbol{d}^{\mathrm{en}}(\boldsymbol{e}) := -\boldsymbol{\mathcal{E}}\cdot\boldsymbol{\nabla}\varphi \tag{17b}$$

$$\mu_{\mathrm{Li}} = \mu_{\mathrm{Li}}^{\mathrm{en}}(c_{\mathrm{Li}},\theta) := \mu_{\mathrm{Li}}^{0} - R\theta_0\log\left(\tilde{c}'_{\mathrm{Li},0}\right) + R\theta\log\left(\tilde{c}_{\mathrm{Li}}\right) \tag{17c}$$

$$\mu_{\mathrm{X}} = \mu_{\mathrm{X}}^{\mathrm{en}}(c_{\mathrm{X}},\theta) := \mu_{\mathrm{X}}^{0} - R\theta_0\log\left(\tilde{c}'_{\mathrm{X},0}\right) + R\theta\log\left(\tilde{c}_{\mathrm{X}}\right) \tag{17d}$$

It appears that the initial values of $\boldsymbol{\sigma}$, μ_{Li} and μ_{X} are $\boldsymbol{\sigma}^{\mathrm{en}}(\boldsymbol{0},\theta_0) = \boldsymbol{0}$, $\mu_{\mathrm{Li}}^{\mathrm{en}}(c_{\mathrm{Li},0},\theta_0) = \mu_{\mathrm{Li}}^{0}$ and $\mu_{\mathrm{X}}^{\mathrm{en}}(c_{\mathrm{X},0},\theta_0) = \mu_{\mathrm{X}}^{0}$.

The dissipative variables $\boldsymbol{j}_{\mathrm{Li}}$, $\boldsymbol{j}_{\mathrm{X}}$ and $\boldsymbol{q}$ are chosen as

$$\boldsymbol{j}_{\mathrm{Li}}(c_{\mathrm{Li}},\boldsymbol{e}) = -\boldsymbol{M}_{\mathrm{Li}}(c_{\mathrm{Li}})\cdot\boldsymbol{\nabla}\mu_{\mathrm{Li}} - F\boldsymbol{M}_{\mathrm{Li}}(c_{\mathrm{Li}})\cdot\boldsymbol{\nabla}\varphi \tag{18a}$$

$$\boldsymbol{j}_{\mathrm{X}}(c_{\mathrm{X}},\boldsymbol{e}) = -\boldsymbol{M}_{\mathrm{X}}(c_{\mathrm{X}})\cdot\boldsymbol{\nabla}\mu_{\mathrm{X}} + F\boldsymbol{M}_{\mathrm{X}}(c_{\mathrm{X}})\cdot\boldsymbol{\nabla}\varphi \tag{18b}$$

$$\boldsymbol{q}(\theta) = -\boldsymbol{K}\cdot\boldsymbol{\nabla}\theta \tag{18c}$$

where the isotropic mobility and thermal conductivity tensors are defined as:

$$\boldsymbol{M}_{\mathrm{Li}}(c_{\mathrm{Li}}) = \eta_{\mathrm{Li}}\rho^{\mathrm{F}}\frac{c_{\mathrm{Li}}[c_{\mathrm{Li,sat}} - c_{\mathrm{Li}}]}{c_{\mathrm{Li,sat}}^2}\boldsymbol{I} \tag{19a}$$

$$\boldsymbol{M}_{\mathrm{X}}(c_{\mathrm{X}}) = \eta_{\mathrm{X}}\rho^{\mathrm{F}}\frac{c_{\mathrm{X}}[c_{\mathrm{X,sat}} - c_{\mathrm{X}}]}{c_{\mathrm{X,sat}}^2}\boldsymbol{I} \tag{19b}$$

$$\boldsymbol{K} = k\boldsymbol{I} \tag{19c}$$

In these expressions, η_α is the mobility coefficient of the species α for α = Li,X. Obviously, we have introduced the simplification that there is no (constitutive) coupling between the diffusion of Li^+ and X^-. Moreover, Eqs. (19a)–(19b) differ from Eq. (8a) principally in the sense that the mobilities vanish when $c_\alpha = 0$ or $c_\alpha = c_{\alpha,\mathrm{sat}}$, cf. Kaessmair et al. (2021). Further, k is the isotropic thermal conductivity.

Finally, using Faraday's law of electrolysis (while exploiting (18a) and (18b)), we derive the constitutive relation for the current density:

$$\boldsymbol{i} = F[\boldsymbol{j}_{\mathrm{Li}} - \boldsymbol{j}_{\mathrm{X}}] = -F\boldsymbol{M}_{\mathrm{Li}}\cdot\boldsymbol{\nabla}\mu_{\mathrm{Li}} + F\boldsymbol{M}_{\mathrm{X}}\cdot\boldsymbol{\nabla}\mu_{\mathrm{X}} - \boldsymbol{\mathcal{K}}\cdot\boldsymbol{\nabla}\varphi \tag{20}$$

where we introduced the ionic conductivity $\boldsymbol{\mathcal{K}} := F^2[\boldsymbol{M}_{\mathrm{Li}} + \boldsymbol{M}_{\mathrm{X}}]$.

3.3. Interior boundaries

The fibre/electrolyte interfaces, denoted Γ_{fe}, represent interior boundaries. We assume that the displacement field $\boldsymbol{u}$ is continuous across Γ_{fe} (i.e. perfectly bonded). However, due to the redox reactions in the close vicinity of the interface, μ_{Li}, φ and θ may be discontinuous across Γ_{fe}, whereas $j_{\mathrm{Li},n}$ is continuous across Γ_{fe}. The discontinuities in μ_{Li} and φ are modelled as linear interface relations involving the "electric resistance" which turns to have a model structure that is similar to a linearized Butler–Volmer relation. With respect to the ion flux we assume that $j_{\mathrm{Li},n}(= j_{\mathrm{Li},n}^{\mathrm{e}}) := \boldsymbol{j}_{\mathrm{Li}}\cdot\boldsymbol{n}$, where $\boldsymbol{n}$ is the normal on Γ_{fe} pointing from the electrolyte domain Ω_{e} into the fibre domain Ω_{f}, is governed constitutively by an interface mobility $\bar{M}$ such that

$$j_{\mathrm{Li},n}(\boldsymbol{x}) = -\bar{M}[\![\mu'_{\mathrm{Li}}]\!](\boldsymbol{x}) = -\bar{M}[\![\mu_{\mathrm{Li}}]\!](\boldsymbol{x}) - F\bar{M}\left[\boldsymbol{\Phi}^- - \varphi^{\mathrm{e}}\right],\ \boldsymbol{x}\in\Gamma_{\mathrm{fe}} \tag{21}$$

In Eq. (21), we introduced the jump operator $[\![\bullet]\!](\boldsymbol{x}) := \bullet(\boldsymbol{x}^{\mathrm{f}}) - \bullet(\boldsymbol{x}^{\mathrm{e}})$ and $\boldsymbol{x}^{\mathrm{f}} := \lim_{\epsilon\downarrow 0}[\boldsymbol{x} + \epsilon\boldsymbol{n}]$, $\boldsymbol{x}^{\mathrm{e}} := \lim_{\epsilon\downarrow 0}[\boldsymbol{x} - \epsilon\boldsymbol{n}]$. Moreover, we utilized the definition $[\![\mu'_{\mathrm{Li}}]\!] = [\![\mu_{\mathrm{Li}}]\!] + F\left[\boldsymbol{\Phi}^- - \varphi^{\mathrm{e}}\right]$ (commonly referred to as the electrochemical potential[6]), where $\varphi^{\mathrm{e}} := \varphi(\boldsymbol{x}^{\mathrm{e}})$ is evaluated in the electrolyte at the fibre–electrolyte interface. The current density flux $i_n := \boldsymbol{i}\cdot\boldsymbol{n}$ across the interface Γ_{fe} is defined as

$$i_n = F[j_{\mathrm{Li},n} - \underbrace{j_{\mathrm{X},n}}_{=0}] = -F\bar{M}[\![\mu_{\mathrm{Li}}]\!] - \bar{\mathcal{K}}\left[\boldsymbol{\Phi}^- - \varphi^{\mathrm{e}}\right]\ \text{on}\ \Gamma_{\mathrm{fe}} \tag{22}$$

where we introduced the assumption $j_{\mathrm{X},n}(\boldsymbol{x}^{\mathrm{e}}) = 0$, $\boldsymbol{x}\in\Gamma_{\mathrm{fe}}$, i.e. the transport of X^- is blocked at the fibre–electrolyte interface. Further, we introduced the interface ionic conductivity $\bar{\mathcal{K}} := F^2\bar{M}$. Next, we introduce the constitutive assumption for $d_n(= d_n^{\mathrm{e}}) := \boldsymbol{d}\cdot\boldsymbol{n}$

$$d_n = -\bar{\mathcal{E}}\left[\boldsymbol{\Phi}^- - \varphi^{\mathrm{e}}\right]\ \text{on}\ \Gamma_{\mathrm{fe}} \tag{23}$$

where $\bar{\mathcal{E}}$ is the interface permittivity.

With respect to the thermal conditions, we evaluate the thermal energy balance at the interface (cf. Eqs. (1c) and (12e)). Firstly, we introduce the normal components of the heat flux vector as $q_n^{\mathrm{f}} := \boldsymbol{q}^{\mathrm{f}}\cdot\boldsymbol{n}^{\mathrm{f}}$ and $q_n^{\mathrm{e}} := \boldsymbol{q}^{\mathrm{e}}\cdot\boldsymbol{n}^{\mathrm{e}}$, where (once again) we note that $\boldsymbol{n}^{\mathrm{e}} = -\boldsymbol{n}^{\mathrm{f}} := \boldsymbol{n}$. The balance equation including the interface may then be expressed as

$$-q_n^{\mathrm{f}} - q_n^{\mathrm{e}} + i_n[\![\varphi]\!] + j_{\mathrm{Li},n}[\![\mu_{\mathrm{Li}}]\!] = 0 \tag{24}$$

where we used that $j_{\mathrm{Li},n}^{\mathrm{e}} = -j_{\mathrm{Li},n}^{\mathrm{f}} := j_{\mathrm{Li},n}$ and $i_n^{\mathrm{e}} = -i_n^{\mathrm{f}} := i_n$, i.e. the normal component of $\boldsymbol{j}_{\mathrm{Li}}$, as well as of $\boldsymbol{i}$, are continuous across the interface. Now, inserting the *ansatz*

$$q_n^{\mathrm{f}} = -\bar{q}_n + \frac{1}{2}\Delta q_n,\ q_n^{\mathrm{e}} = \bar{q}_n + \frac{1}{2}\Delta q_n \tag{25}$$

into (24), we obtain

$$\Delta q_n = i_n[\![\varphi]\!] + j_{\mathrm{Li},n}[\![\mu_{\mathrm{Li}}]\!] = i_n\left[[\![\varphi]\!] + \frac{1}{F}[\![\mu_{\mathrm{Li}}]\!]\right] \tag{26}$$

where we used the identity $i_n = F\,j_{\mathrm{Li},n}$. The quantity Δq_n represents the heat absorbed at the interface (i.e. "heat sink"), and it is noted that the expression in Eq. (26) follows directly from the heat balance and does not require any additional constitutive assumption. This is in line with conventional battery modelling frameworks, see e.g. Newman and Thomas-Alyea (2004).

Finally, we adopt a standard expression for the heat transfer across the interface (from the fibre to the electrolyte) in terms of the temperature jump

$$\bar{q}_n = -\bar{\mathcal{K}}^{\mathrm{th}}[\![\theta]\!] \tag{27}$$

where $\bar{\mathcal{K}}^{\mathrm{th}}$ is the interface transfer resistance coefficient (or effective layer conductance).

Remark 4. The interface's contribution to the dissipation inequality may be included in the formulation, e.g. in the case of mechanical damage (cf. Singh and Pal (2020) and Rezaei et al. (2021)).

[4] Piezoelectric effects are disregarded (as is commonly done in the electrochemistry literature).

[5] Both $c_{\mathrm{Li,ref}}$ and $c_{\mathrm{X,ref}}$ are chosen as 1 mol kg^{-1}. This value is obtained from setting $\rho^{\mathrm{F}}c_{\alpha,\mathrm{ref}} = 1$ molar (or 10^3 mol m^{-3}) and $\rho^{\mathrm{F}} = 10^3$ kg m^{-3}.

[6] In analogy with Newman and Thomas-Alyea (2004) and Salvadori et al. (2015), we use the definition of the electrochemical potential, where the effect of the electric potential on the chemical potential is accounted for.

3.4. Exterior boundary

The entire external boundary comprises $\Gamma_{\text{ext}} = \sum_{i=1}^{3} \cup \Gamma_{\text{ext},i}$ and the collector boundary Γ_+. With respect to the mechanical conditions, related to displacements ($\boldsymbol{u}$) and tractions ($\boldsymbol{\sigma}_n = \boldsymbol{\sigma} \cdot \boldsymbol{n}$), we assume that:

$$u_1 = 0,\ \sigma_{n,2} = 0 \text{ on } \Gamma_{\text{ext},2} \cup \Gamma_{\text{ext},3} \tag{28a}$$

$$\boldsymbol{\sigma}_n = \boldsymbol{0} \text{ on } \Gamma_{\text{ext},1} \cup \Gamma_+ \tag{28b}$$

These conditions are motivated by the fact that the studied (part of the) lamina will in practice constitute a layered plate structure (cf. Carlstedt et al. (2020)).

Further, for chemical conditions related to ion flux ($j_{\text{Li},n} = \boldsymbol{j}_{\text{Li}} \cdot \boldsymbol{n}$, $j_{\text{X},n} = \boldsymbol{j}_{\text{X}} \cdot \boldsymbol{n}$), we set:

$$j_{\text{Li},n} = -F\bar{\mathcal{M}}\left[\Phi^+ - \varphi^{\text{e}}\right] \text{ on } \Gamma_+ \tag{29a}$$

$$j_{\text{Li},n} = 0 \text{ on } \Gamma_{\text{ext},2} \cup \Gamma_{\text{ext},3} \tag{29b}$$

$$j_{X,n} = 0 \text{ on } \Gamma_{\text{ext},2} \cup \Gamma_{\text{ext},3} \cup \Gamma_+ \tag{29c}$$

The assumed chemical conditions are motivated by the fact that the ion flux occurs between the Li-metal and fibres (i.e. mainly in the x_2-direction) and that the height of the studied unit corresponds to the thickness of the electrode lamina, cf. Fig. 2b.

With respect to the electrical conditions, related to the electric flux density (d_n), we set:

$$d_n = -\bar{\mathcal{E}}\left[\Phi^+ - \varphi^{\text{e}}\right] \text{ on } \Gamma_+ \tag{30a}$$

$$d_n = 0 \text{ on } \Gamma_{\text{ext}} \tag{30b}$$

where Γ_{ext} denotes all exterior boundaries except Γ_+. It is noted that Φ^+ is a spatially constant value in the collector (Li-metal) just outside Γ_+ and φ^{e} is the electrolyte potential along Γ_+. Moreover, we assume that Φ^+ is prescribed at 0 V.

Finally, the thermal conditions related to the heat flux ($q_n = \boldsymbol{q} \cdot \boldsymbol{n}$) are defined as:

$$q_n = 0, \text{ on } \Gamma_{\text{ext},2} \cup \Gamma_{\text{ext},3} \cup \Gamma_+ \tag{31a}$$

$$q_n = -\bar{\mathcal{K}}^{\text{th}}_{\text{ext}}[\theta_{\text{ext}} - \theta] \text{ on } \Gamma_{\text{ext},1} \tag{31b}$$

In Eq. (31b) we assume a convective heat flux where $\bar{\mathcal{K}}^{\text{th}}_{\text{ext}}$ is the heat transfer coefficient and θ_{ext} is the external temperature. These conditions are motivated from experimental studies, Asp et al. (2021) and Johannisson et al. (2018). Finally, it should be noted that we neglect heat that is generated or absorbed along Γ_+.

4. Model geometry, loading conditions and parameter values

4.1. FE-model geometry and loading conditions

The model geometry and (triangular) finite element (FE) mesh are presented in Fig. 3a. An SEM-image of the corresponding cross-section (from Carlstedt et al., 2022a) is provided in Fig. 3b, for comparison. The fibre volume fraction (V_{f}) is set to $V_{\text{f}} = 0.45$, and the dimensions and fibre volume fraction are motivated by experimental measurements in Johannisson et al. (2018) and Carlstedt et al. (2022a).

The numerical implementation is done in the commercial FE software COMSOL Multiphysics version 5.4. The time-incremental weak format of the governing equations (presented in Appendix B) are set up and solved in a monolithic fashion, i.e. without any staggering between the different physical mechanisms. The polynomial order of the triangular Lagrange elements (Fig. 3a) used for the various primary fields in the fibres and the SBE domains are presented in Appendix D.1. It should be noted that the dependent variables in the respective domains (fibre/SBE) are defined independently. Hence, no interface elements are used at the interior boundaries.

To illustrate the utilized convention for charge/discharge conditions, we provide a schematic illustration of the studied CF-SBE electrode half-cell in Fig. 3c. The corresponding electric potential and applied mass specific current versus time are shown in Fig. 3d. We then assume that the fibres are lithiated during discharge, i.e. Li-ions move from the Li-metal to the fibres. On the other hand, the fibres are delithiated during the charge phase, i.e. Li-ions move from the fibres to the Li-metal. Only galvanostatic conditions are considered in this study.

With respect to the mechanical loading condition in the x_3-direction, we considered the case of generalized plane stress ($\epsilon_{33}(x_1, x_2, t) = \bar{\epsilon}_{33}(t)$), defined by the condition:

$$N_{33}(t) := \int_{\Omega} \sigma_{33}(\bullet, t)\, \mathrm{d}S = 0 \tag{32}$$

Here we note that Ω defines a surface in 2D and that an extra condition is needed to compute $\bar{\epsilon}_{33}(t)$ as part of the FE-problem.

With respect to the electrochemical loading conditions we apply a constant (dis)charge current, defined as

$$I^- = \frac{i^{\text{f}}_m m^{\text{f}}}{l} = i^{\text{f}}_m A^{\text{f}} \rho \tag{33}$$

where I^- is the total applied current per unit length, i^{f}_m is the applied mass-specific current and m^{f} is the fibre mass of the unit cell.

4.2. Parameter values

The parameter values used in the analysis are listed in Table D.2 (in Appendix D). The particular choice of relevant values is discussed in Carlstedt et al. (2020, 2022b). The reference/standard value of μ^0_{Li} for Li in the fibres is based on measurements by Kjell et al. (2013), while $\mu^0_{\text{Li}} = 0$ in the electrolyte. As to the Li-concentration dependent elastic properties of the fibres, we set $L_\perp(c_{\text{Li}}) = L^0_\perp[1 + 1.07\bar{c}_{\text{Li}}]$ in accordance with measurements by Duan et al. (2021). Moreover, the effective values of Lamé's parameters (L, G) and ion mobilities (η_α) for the SBE are based on estimated values for a porosity of $\phi = 0.4$ (cf. Carlstedt et al. (2022b) and Fig. 1b). It is also noted that the total applied current (I^-) is defined based on the mass-specific current i^{f}_m (cf. (33)). As reference state we utilize $i^{\text{f}}_m = 168$ A kg^{-1} of fibres, which corresponds to the electric current needed to discharge the carbon fibre electrode half-cell in approximately 1 h (i.e. C-rate = 1), based on measurements by Jacques et al. (2013a). Further, $c_{\text{Li,max}}$[7] and the insertion induced expansion coefficients ($\alpha^{\text{ch}}_\perp$, $\alpha^{\text{ch}}_\parallel$) of the fibre are based on measurements for this particular current, cf. Jacques et al. (2013a). For simplicity, these values are not altered for different values of i^{f}_m. Finally, we set the saturation (maximum) concentrations in the electrolyte to $c_{\alpha,\text{sat}} = 3$ mol kg^{-1} (Nyman et al., 2008).

The interface mobility is set as: $\bar{M} = i_0/[R\theta_0 F]$. The exchange current density (i_0) is assumed constant for simplicity and is based on measurements by Kjell et al. (2013). Further, the interface permittivity is chosen as $\bar{\mathcal{E}} = \varepsilon/\delta$, where δ is the assumed thickness of the electric double layer. The relative permittivity is set to $\varepsilon_r = 10$, cf. Fontanella and Wintersgill (1988) and Ganser et al. (2019), and the thickness of the electric double layer is set to 0.5 nm, cf. Ganser et al. (2019) and Braun et al. (2015).

The thermal expansion coefficients of the fibres ($\alpha^{\text{th}}_\perp$, $\alpha^{\text{th}}_\parallel$) and SBE ($\alpha^{\text{th}}$), are based on data from Bowles and Tompkins (1989). Moreover, the thermal conductivity ($k_\parallel, k_\perp$), volume specific heat capacity (C_{v}) and electronic conductivity (κ^{f}) of the carbon fibres are based on measurements from the supplier (Torayca, 2018). The thermal conductivity (k) and volume specific heat capacity (C^{e}_{v}) of the SBE are based on data from Zantout and Zhupanska (2010). It should be noted that the thermal properties of the SBE are based on conventional

[7] The maximum Li-concentration in the fibres is estimated as $c_{\text{Li,max}} = C^{\text{f}}3600/F$, where C^{f} is the assumed specific capacity, cf. Jacques et al. (2013a).

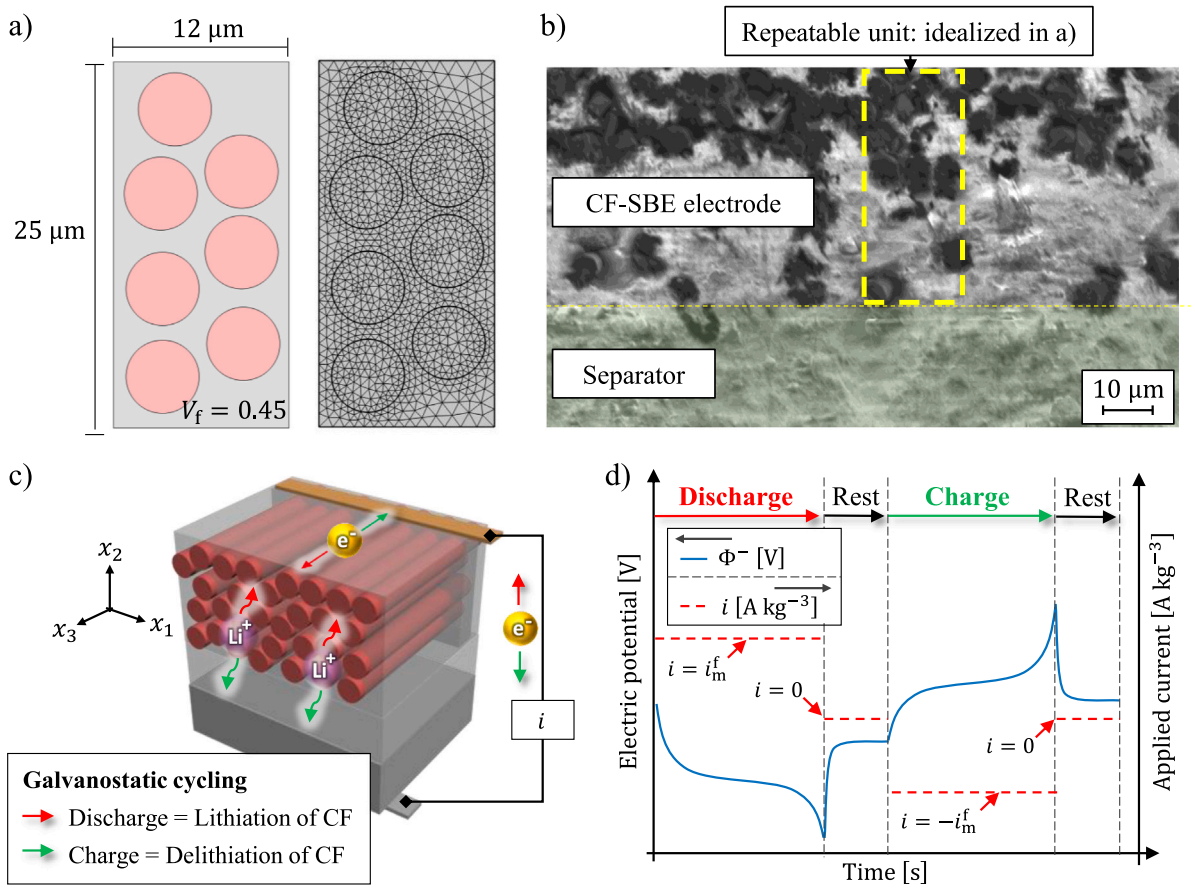

Fig. 3. (a) Model geometry and triangular element mesh for the FE-model set-up in COMSOL Multiphysics. (b) SEM-image of a cross-section of the studied half-cell, from Carlstedt et al. (2022a). (c) Schematic illustration of the studied CF-SBE electrode half-cell. (d) Electric potential and applied current density versus time, illustrating the utilized convention for charge/discharge conditions.

polymer systems for carbon fibre reinforced polymers (due to lack of experimental data for the developed SBE systems (Ihrner et al., 2017; Schneider et al., 2019)). Further, the assumed fibre-SBE interface heat transfer coefficient ($\bar{\kappa}^{\text{th}}$) is based on data from Macedo and Ferreira (2003) for polymer-based carbon fibre composites. Moreover, the fibre length l is allowed to vary between 0.1–0.2 m in the parametric study performed in Section 5.4. For the remaining studies we set to $l = 0.1$ m. The heat exchange coefficient with the surroundings ($\bar{\kappa}^{\text{th}}_{\text{ext}}$) and the volume specific heat capacity of the SBE (C_v^e) are allowed to vary between 1–10 W m^{-2} K^{-1} and 10^5-10^7 J m^{-3} K^{-1}, respectively, in the parametric study performed in Section 5.5. For the remaining studies (i.e. excluding the parametric study), we set $\bar{\kappa}^{\text{th}}_{\text{ext}} = 1$ W m^{-2} K^{-1} (cf. Gigliotti et al. (2011) and Xu et al. (2022)) and $C_v^e = 2 \cdot 10^6$ J m^{-3} K^{-1} (cf. Zantout and Zhupanska (2010)).

Finally, we note that as initial state for the simulations we set $\tilde{c}_{\text{Li},0} = 0.01$ in the fibres, $\tilde{c}_{\alpha,0} = 1$ in the SBE and $\theta_0 = 293.15$ K.

5. Results and discussion

5.1. A complete discharge/charge cycle under galvanostatic control

To demonstrate that the developed framework can predict the coupled thermo–electro–chemo–mechanical behaviour, we perform a complete discharge/charge cycle under galvanostatic control with a current of $i_m^f = 168$ A kg^{-1} of fibres. Results from this (dis)charge process are presented in Fig. 4. The applied current corresponds to a (dis)charge time of approximately 1 h, cf. Jacques et al. (2013a). After the discharge and charge process respectively, the current is set to zero for 500 s to allow the cell to rest. During discharge, the Li-ions move from the Li-metal to the fibres via the electrolyte and insert into the fibres while the electrons move via the external circuit, see Fig. 4a. This alters the electric potential (Φ^-) as well as the Li-concentration in the electrolyte ($\tilde{c}_{\text{Li}}^e$) and the fibres ($\tilde{c}_{\text{Li}}^f$), as shown in Fig. 4b.

The Li-ions enter the fibres via the fibre/electrolyte interface and cause the fibres to expand, generating internal stresses and strains (Fig. 4c). Due to the fact that the free expansion of the fibres is hindered by the surrounding SBE, in addition to the assumed mechanical boundary conditions, this results in a continuous increase of the compressive stress state in the fibre during discharge (i.e. lithiation). In the SBE on the other hand, the stress state depend significantly on the assumed fibre arrangement and boundary conditions, and are both of tensile and compressive nature. During charge, the mass and charge transport processes are reversed (compared with the discharge process). This causes the stresses to decrease (based on the assumption of zero stress/strain at $\tilde{c}_{\text{Li}}^f = 0$) as the Li-concentration in the fibres reduces.

The transport of charged species and electrochemical reactions generate (or absorb) heat, which alters the temperature (Fig. 4d). Heat is generated due to transport of charged species during both the discharge and charge processes. How the average temperature evolves within the half-cell is presented in Fig. 4d. It is noted that the temperature increases initially before it reaches a “plateau”. Further, the temperature distribution in the through thickness direction (x_2-direction) is found to be negligible throughout the complete (dis)charge process. This is considered reasonable given the dimensions of the studied geometry (thickness of electrode 25 μm). Moreover, it is noted that the temperature inside the material quickly returns to the temperature of the surroundings when the current is set to zero (Fig. 4d). Finally, we observe that the average temperature during charge is slightly higher as compared with the case of discharge.

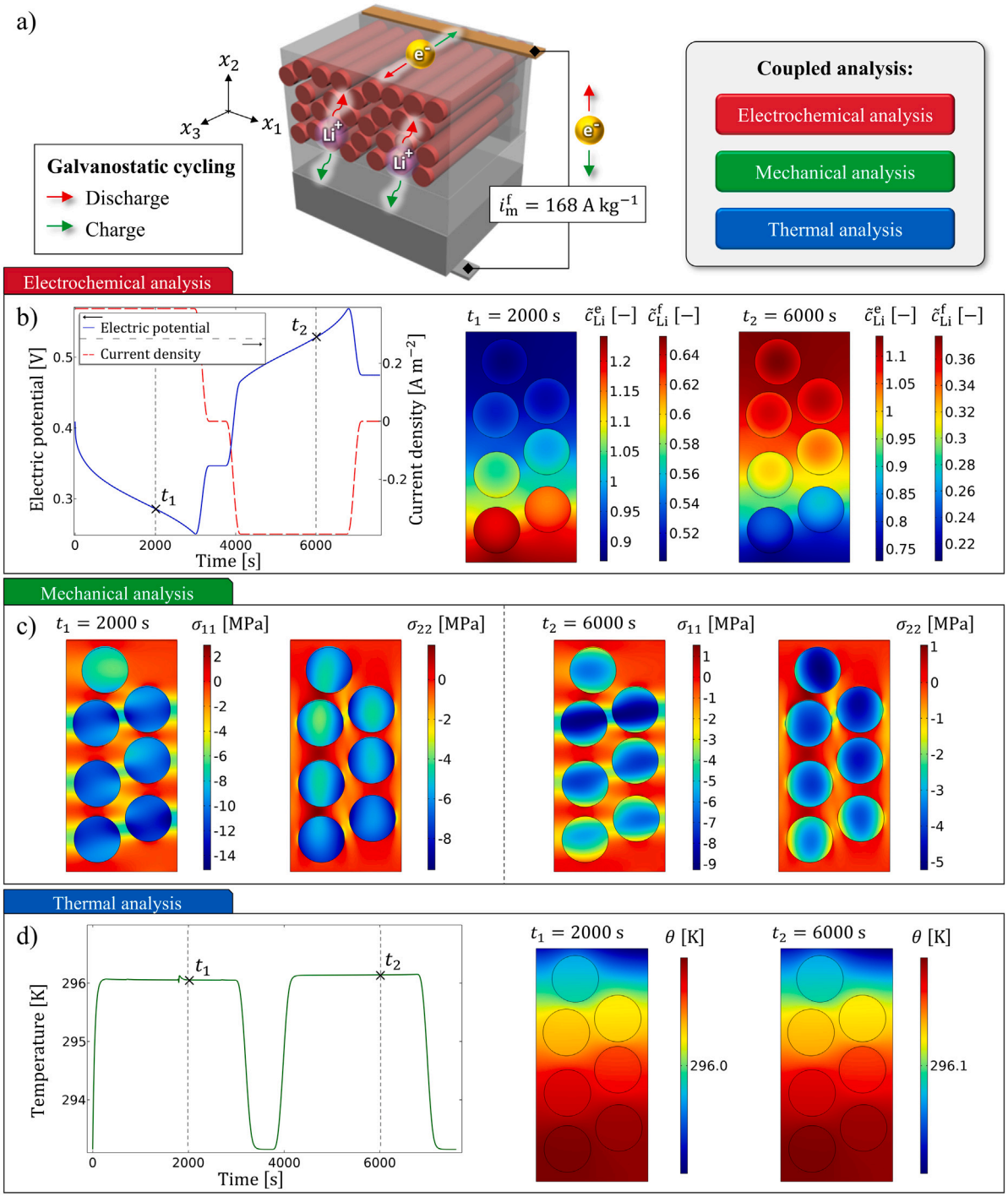

Fig. 4. (a) A complete discharge/charge cycle under galvanostatic control with $i_m^f = 168$ A kg^{-1} of fibres is performed. (b) Electric potential (Φ^-) and current density (i_n) versus time, and normalized Li-concentration in the SBE ($\tilde{c}_{Li}^e$) and fibres ($\tilde{c}_{Li}^f$) at time instances $t_1 = 2000$ s and $t_2 = 6000$ s. (c) In-plane stress components (σ_{11}, σ_{22}) at t_1 and t_2. (d) Average temperature inside the half-cell versus time, and temperature distribution (θ) at t_1 and t_2.

Finally, we quantify the error associated with the simplification made: assuming a constant electric potential in the fibres while approximating a heat generation in the fibres due the electric current (cf. Section 3.1.3). For the given applied current the electric field component e^f is estimated (using Eq. (9)) to be approximately 0.26 V per metre. Hence, over the fibre length $l = 0.1$ m this corresponds to a voltage drop of 0.026 V. This can be compared with the electric potential presented in Fig. 4b, which is ranging from approximately 0.25 to 0.55 V. It is evident that this contribution is small in comparison with the approximated electric potential. Further, in the case of a so-called full-cell, i.e. when the Li-metal is replaced with a positive electrode (see e.g. Asp et al. (2021)), this effect will be even smaller as the operating voltage is further increased (roughly 2 - 3.5 V). However, we note that this effect should be considered to accurately estimate the power delivered by the battery, or to quantify the energy efficiency during operation.

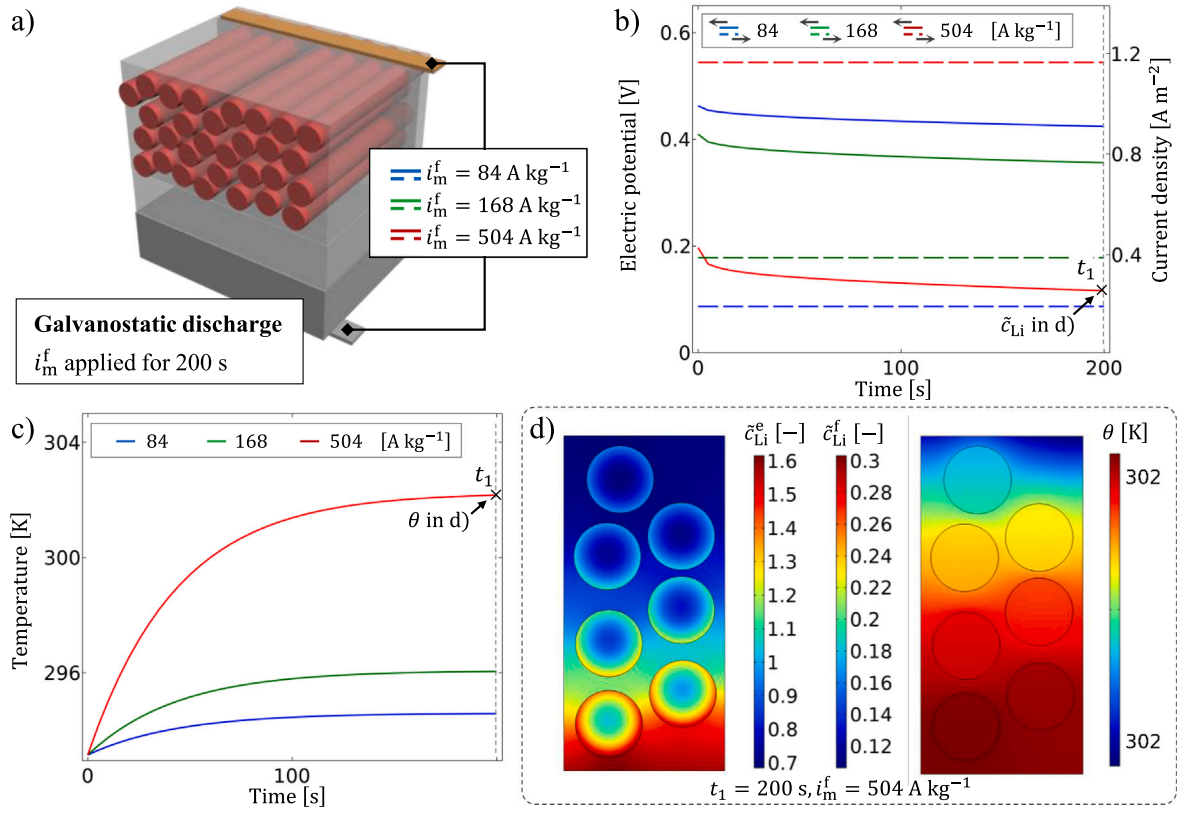

Fig. 5. (a) Galvanostatic discharge (for 200 s) at different applied currents: i_m^f = 84, 168, 504 A kg^{-1} of fibres are performed. (b) Electric potential (Φ^-) and current density (i_n) versus time. (c) Average temperature inside the half-cell versus time. (d) Normalized Li-concentrations ($\tilde{c}^e_{Li}$, $\tilde{c}^f_{Li}$) and temperature distribution (θ) at time t_1 = 200 s (i_m^f = 504 A kg^{-1}).

5.2. Effect of (dis)charge rate/applied electric current

The influence of (dis)charge rate, i.e. applied electric current, under galvanostatic discharge is studied. The computational results for a 200 s discharge pulse at currents: i_m^f = 84, 168, 504 A kg^{-1} of fibres (which corresponds to an assumed discharge time of 2, 1 and 0.33 h, respectively) are presented in Fig. 5. The initial Li-concentration in the fibres is set to $\tilde{c}_{Li}$ = 0.01. In Fig. 5b, the electric potential and applied current density versus time are shown for the three cases. It is evident that the electric potential is highly influence by the current density, as expected. Further, in Fig. 5c the temperature evaluation for the studied discharge currents are presented. Since the generated heat associated with the electronic current in the fibres depends on the applied current i_m^f (cf. Eq. (9)), the temperature at which an equilibrium between heat generated and heat exchange is reached will increase for larger currents. For example, at the simulated discharge current i_m^f = 504 A kg^{-1} (discharge time 0.33 h, or C-rate = 3) the temperature increase is approximately 9 degrees and stabilizes after approximately 200 s. In Fig. 5d, the normalized Li-concentrations and temperature at time t_1 = 200 s for i_m^f = 504 A kg^{-1} of fibres are presented. The temperature distribution inside the material is found to be negligible while the variation in concentrations is significant both in the SBE and fibres. The large variations in concentrations is due to the transport properties of the constituents and the applied current.

5.3. Coupling terms associated with the thermal interaction

With respect to coupling terms linked to the thermal interaction with the electrochemical and mechanical processes, we identify the following relevant couplings: (i) The electric potential Φ^- is correlated with the chemical potential of Li in the fibres, which depends on the mechanical strain, Li-concentration and temperature: $\mu_{Li}(\boldsymbol{\epsilon}, c_{Li}, \theta)$ in Ω_f and $\mu_\alpha(c_\alpha, \theta)$ in Ω_e, cf. (6b) and (17c)–(17d); (ii) The mechanical stress field depends on the mechanical strain, Li-concentration and temperature, i.e. $\boldsymbol{\sigma}(\boldsymbol{\epsilon}, c_{Li}, \theta)$ in Ω_f and $\boldsymbol{\sigma}(\boldsymbol{\epsilon}, \theta)$ in Ω_e, cf. Eqs. (6a) and (17a). To study these coupling terms we repeat the galvanostatic discharge pulse at i_m^f = 168 and 504 A kg^{-1} (for 200 s) for the following two cases:

- **Case 1:** Temperature dependence of the chemical potentials (μ_α) included (i.e. problem is solved as described in Section 3)
- **Case 2:** Temperature dependence of the chemical potentials neglected. This is achieved by defining the chemical potentials (Eqs. (6b), (17c) and (17d)) in terms of a reference temperature corresponding to the starting temperature of the simulation (i.e. 293.15 K)

In Fig. 6a–b, the electric potential (Φ^-) and the average temperature in the half-cell, versus time, are presented for the two cases presented above. It is clear that temperature dependence of the chemical potentials only has minor effect on both electric potential and temperature evolution. The effect becomes more pronounced when the temperature change increases due to the increased electric loading (Fig. 6b), as expected. It should be noted that idealized definitions of the chemical potentials are used.

In Fig. 6c–d, the in-plane strain components in the x_1-direction (cf. Eqs. (3a), (14) and (3b)) at time t_1 = 200 s are presented for Case 1 and the two studied electric loading scenarios. The thermal strains (ϵ_{11}^{th}) in the fibres are found to be orders of magnitude lower compared with the other strain components. However, the magnitude of the thermal strains in the SBE are found to be comparable with the insertion induced strains, in particular for large temperature increase. Hence, in this case of large temperature increase (or decrease), e.g. due to large applied current and/or large variations in the surrounding temperature, the thermal strains in the SBE may have noticeable effect on the resulting strain level. Finally, we emphasize that the stiffness

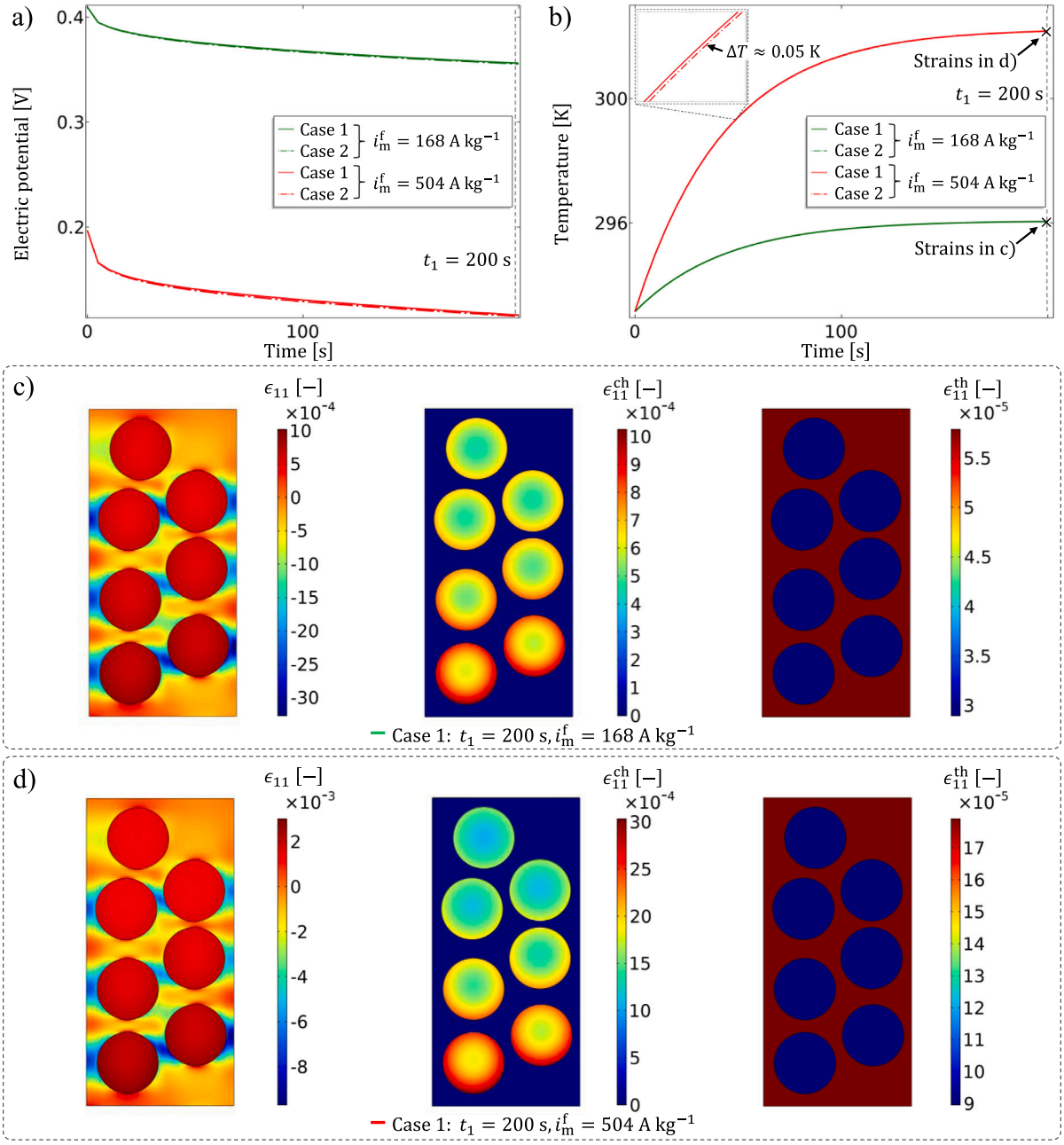

Fig. 6. Galvanostatic discharge cycle at $i_m^f = 168$ and 504 A kg^{-1} of fibres. (a) Electric potential (Φ^-) and (b) average temperature inside the material versus time for the cases: 1. $\mu_\alpha(\epsilon, c_{Li}, \theta)$, 2. $\mu_\alpha(\epsilon, c_{Li}, \theta_0)$. (c)–(d) In-plane strain components in the x_1-direction (total ϵ_{11}, chemical ϵ_{11}^{ch} and thermal ϵ_{11}^{th} strain), at time instance $t_1 = 200$ s for the case of $i_m^f = 168$ and 504 A kg^{-1} of fibres, respectively.

of conventional polymers, as well as the ion conductivity of the electrolyte, are known to be highly temperature dependent (Gigliotti et al., 2011; Ihrner et al., 2017). However, these dependencies are currently not accounted for.

5.4. Significance of the individual terms in the thermal energy balance

To assess the influence of the individual contributions to the thermal energy balance, we identify and denote the respective terms associated with heat generation and/or absorption in Eqs. (1c), (11), (26) and (12e) as follows:

- $\xi_1 = \boldsymbol{j}_{Li} \cdot \nabla \mu_{Li}$
- $\xi_2 = \boldsymbol{j}_X \cdot \nabla \mu_X$
- $\xi_3 = F[\boldsymbol{j}_{Li} - \boldsymbol{j}_X] \cdot \nabla \varphi$
- $\xi_4 = \Delta q_n$
- $\xi_5 = Q_{elec}$

It should be noted that ξ_2 and ξ_3 are relevant only in the SBE, whereas ξ_4 relates to the heat generated at the fibre/electrolyte interface and ξ_5 to the electron transport along the fibres. The results are extracted by running six simulations: one simulation where all terms are included ($\sum_i \xi_i$) and five simulations where each individual term is accounted for (ξ_i) while the remaining terms are set to zero.

In Fig. 7, the individual contributions are shown for the case of galvanostatic discharge during 200 s at $i_m^f = 168$ and 504 A kg^{-1} (and fibre length $l = 0.1$ m and 0.2 m). It appears the heat generation associated with ξ_4 is the dominating contribution to the thermal energy balance for low current (Fig. 7a). Further, the resistive (Joule) heating of the fibres (ξ_5) provides a relevant contribution, in particular for large

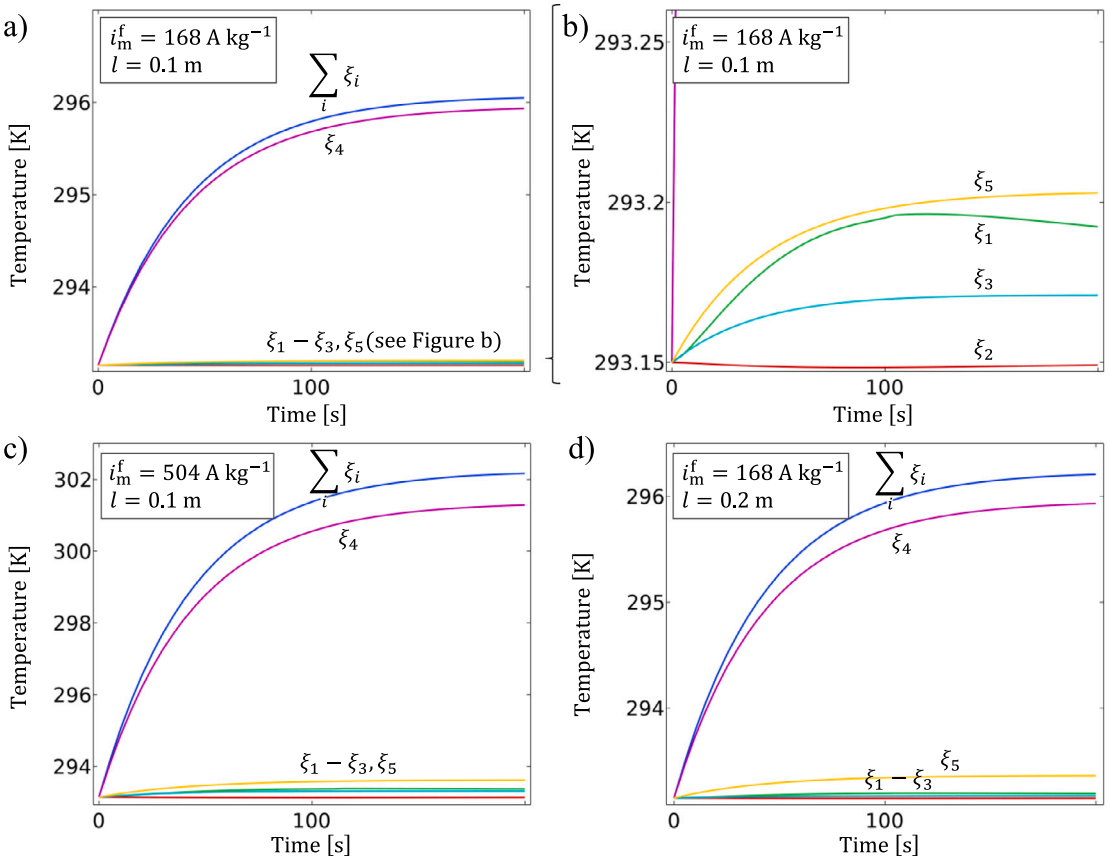

Fig. 7. Galvanostatic discharge for 200 s: (a) The individual contributions to the temperature evolution for $i^f = 168$ A kg^{-1} of fibres and $l = 0.1$ m. (b) Graph only showing the contributions $\xi_1 - \xi_3$ and ξ_5 (Zoom-in). (c) The individual contributions to the temperature evolution for $i^f = 504$ A kg^{-1} of fibres ($l = 0.1$ m). (d) The individual contributions to the temperature evolution for $i^f = 168$ A kg^{-1} of fibres and $l = 0.2$ m.

current (Fig. 7c–d). The remaining contributions are small compared with the dominating terms (cf. Fig. 7b). Further, we note that the contribution associated with ξ_5 is proportional to l^2, where l is the fibre length, cf. Eq. (11). The computed temperature evolution is confirmed qualitatively by results of Schutzeichel et al. (2021), who considered a discharge current corresponding to approximately C-rate = 12 (when setting the fibre length $l = 1$ m) and $\bar{\mathcal{K}}^{\text{th}}_{\text{ext}} = 5$ W m^{-2} K^{-1}. It should be noted that in the case of $i^f_m = 504$ A kg^{-1} and $l = 0.1$ m the electric field component e^f is approximately 0.78 V per metre, which corresponds to a drop in electric potential over the fibre length of 0.078 V. This can be compared with the operating voltage of the half-cell being around 0.2 V. Further, in the case of $i^f_m = 168$ A kg^{-1} and $l = 0.2$ m the corresponding drop is approximately 0.1 V while the operating voltage is around 0.4 V.

5.5. Parametric studies: $\bar{\mathcal{K}}^{th}_{ext}$ and C_v for the SBE

To assess the influence of the boundary condition associated with the convective heat flux (cf. Eq. (31b)), we repeated the galvanostatic discharge process with duration 200 s at $i^f_m = 168$ A kg^{-1} of fibres for different heat transfer coefficients $\bar{\mathcal{K}}^{\text{th}}_{\text{ext}}$ (Fig. 8a). The resulting temperature evolutions are presented in Fig. 8b. It is evident that the temperature increase is highly influenced by the heat transfer coefficient. Further, to illustrate the influence of material properties on the temperature evolution, we re-ran the galvanostatic discharge pulse with different values of the volume specific heat capacity of the SBE (C^e_v) for $\bar{\mathcal{K}}^{\text{th}}_{\text{ext}} = 1$ W m^{-2} K^{-1}. The resulting temperature evolutions are presented in Fig. 8c. As expected, the temperature increase within the material is faster for lower values of C_v. It should be noted that experimental data for the developed SBE systems is largely lacking.

6. Conclusions and outlook to future work

In this work, a fully coupled thermo–electro–chemo–mechanical computational modelling framework for carbon fibre based structural batteries is presented. We thereby extend a previously developed computational framework to account for thermal interaction effects, which means that the energy balance now becomes an additional governing equation. We have limited the numerical studies to galvanostatic conditions.

The numerical results reveal that the dominating source for heat generation during galvanostatic cycling is associated the discontinuities in the electrical and chemical potentials at the fibre/electrolyte interface. For large temperature variations, e.g. due to large (dis)charge current or variations in external temperature, the magnitude of the thermal strains in the SBE are found to be similar to the insertion induced strains. Moreover, it is shown that the temperature change during electrochemical cycling is significantly influenced by the applied current, thermal properties of the constituents and heat exchange with the surroundings.

As to future work, we note that reliable material data for the studied material system (in particular linked to thermal dependencies) are lacking. For example, the effective thermal conductivity of the SBE is (to the authors knowledge) not available in the literature. Moreover, how the stiffness of the SBE depends on the temperature is unknown; hence, this dependence is currently not accounted for. In addition, the effective ion conductivity of the SBE is known to be highly influenced by temperature (Ihrner et al., 2017). Adding such material dependencies is part of future work. Moreover, realistic material geometries are needed when proceeding with more detailed studies, e.g. to study the mechanical damage tolerance or longevity of the material. Further, a more rigorous

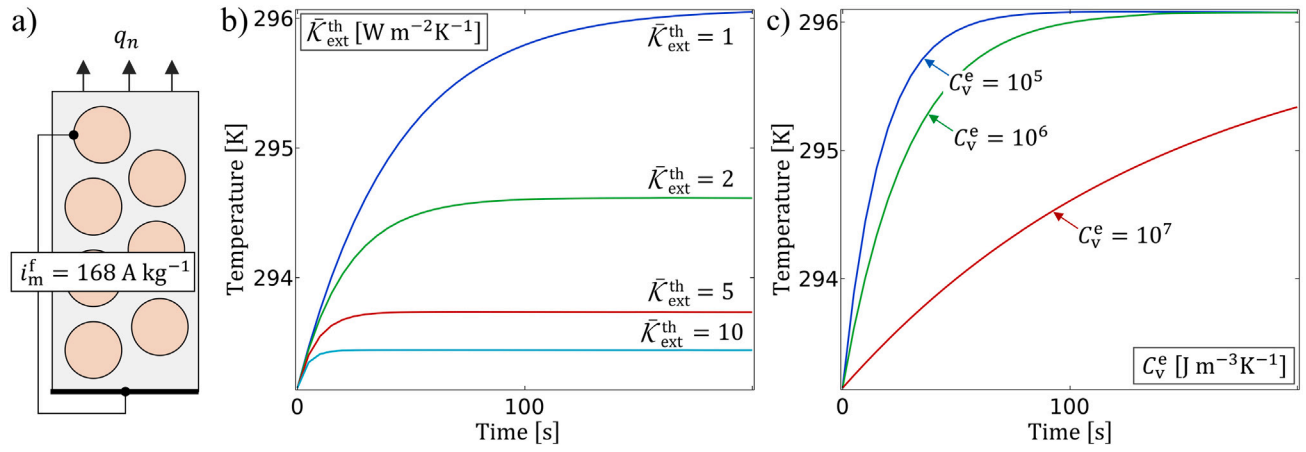

Fig. 8. (a) Galvanostatic discharge (for 200 s) at $i_m^f = 168$ A kg^{-1} of fibres is performed. (b) Temperature evolution for different heat transfer coefficients $\bar{\kappa}_{ext}^{th}$ [W m^{-2} K^{-1}] ($C_v^e = 2 \cdot 10^6$ J m^{-3} K^{-1}), and (c) for different volume specific heat capacity C_v^e [J m^{-3} K^{-1}] of the SBE ($\bar{\kappa}_{ext}^{th} = 1$ W m^{-2} K^{-1}).

approach for dealing with the three dimensional problem is required in order to e.g. estimate the power delivered by the battery or quantify the energy efficiency during operation. In particular, such an approach must account for the different length scales (thickness vs. length/width) involved, e.g. by combining the micro-scale (cross-section) problem with the macro-scale structural problem. Such extension is planned for future work.

CRediT authorship contribution statement

David Carlstedt: Conceptualization, Methodology, Software, Formal Analysis, Writing – original draft, Visualization, Project administration. **Kenneth Runesson:** Conceptualization, Methodology, Writing – original draft, Supervision, Project administration, Funding acquisition. **Fredrik Larsson:** Conceptualization, Methodology, Writing – review & editing, Supervision. **Leif E. Asp:** Conceptualization, Methodology, Writing – review & editing, Supervision, Project administration, Funding acquisition.

Declaration of competing interest

The authors declare that they have no known competing financial interests or personal relationships that could have appeared to influence the work reported in this paper.

Acknowledgements

This project has been funded by USAF contract FA8655-21-1-7038, the Swedish National Space Agency, contract 2020-00256, and the Swedish Research Council (VR) Grant no. 2020-05057, which are gratefully acknowledged. The simulations were performed on resources at Chalmers Centre for Computational Science and Engineering (C3SE) provided by the Swedish National Infrastructure for Computing (SNIC).

Appendix A. Thermodynamics of an electro-chemical-thermal-mechanical system

A.1. Balance of momentum, charge and mass

We consider a (part of a) body that occupies the (arbitrarily chosen) domain $\mathcal{B} \subset \mathbb{R}^3$ with boundary $\partial\mathcal{B} \subset \mathbb{R}^2$. The balance equations of momentum, charge (Gauss' law), and mass read

$$-\boldsymbol{\sigma} \cdot \boldsymbol{\nabla} = \mathbf{0} \qquad \text{in } \mathcal{B} \times \mathbb{R}^+ \tag{A.1a}$$

$$\boldsymbol{d} \cdot \boldsymbol{\nabla} = \rho \sum_\alpha z'_\alpha c_\alpha \qquad \text{in } \mathcal{B} \times \mathbb{R}^+ \tag{A.1b}$$

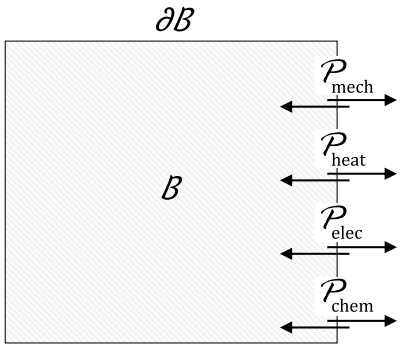

Fig. A.9. Body exchanging energy of electro–chemical–thermal–mechanical nature with the environment.

$$\rho \partial_t c_\alpha + \boldsymbol{j}_\alpha \cdot \boldsymbol{\nabla} = 0 \qquad \text{in } \mathcal{B} \times \mathbb{R}^+ \tag{A.1c}$$

where $\boldsymbol{\sigma}$ is the (symmetric) stress tensor, $\boldsymbol{d}$ is the electric flux density (dielectric displacement) vector and ρ is the bulk density. Further, for any given species α, c_α is the ion concentration, $\boldsymbol{j}_\alpha$ is the ion flux vector, whereas $z'_\alpha = F z_\alpha$ is the specific charge (z_α is the valence number and F is Faraday's constant). To simplify matters, we ignored any volume-specific reaction term in (A.1c).

A.2. Balance of energy

The body may exchange energy of different nature (electrical, chemical, thermal and mechanical) with the environment. The global format of the energy balance reads

$$\int_{\mathcal{B}} \partial_t e \, \mathrm{d}V = \mathcal{P}_{\text{mech}} + \mathcal{P}_{\text{heat}} + \mathcal{P}_{\text{elec}} + \mathcal{P}_{\text{chem}} \tag{A.2}$$

where e (the parametrization of which is discussed later) is the volume-specific internal energy. Referring to Fig. A.9, we define the power supply to the body of mechanical, thermal, electrical and chemical nature as follows:

$$\mathcal{P}_{\text{mech}} = \int_{\mathcal{B}} \boldsymbol{f} \cdot \partial_t \boldsymbol{u} \, \mathrm{d}V + \int_{\partial\mathcal{B}} \boldsymbol{t} \cdot \partial_t \boldsymbol{u} \, \mathrm{d}S \quad \text{with } \boldsymbol{t} := \boldsymbol{\sigma} \cdot \boldsymbol{n}, \tag{A.3a}$$

$$\mathcal{P}_{\text{heat}} = \int_{\mathcal{B}} r \, \mathrm{d}V - \int_{\partial\mathcal{B}} q_n \, \mathrm{d}S \quad \text{with } q_n := \boldsymbol{q} \cdot \boldsymbol{n}, \tag{A.3b}$$

$$\mathcal{P}_{\text{elec}} = \int_{\mathcal{B}} \boldsymbol{i}_{\text{Max}} \cdot \boldsymbol{e} \, \mathrm{d}V, \tag{A.3c}$$

$$\mathcal{P}_{\text{chem}} = -\sum_\alpha \int_{\partial\mathcal{B}} j_{\alpha,n} \mu_\alpha \, \mathrm{d}S \quad \text{with } j_{\alpha,n} := \boldsymbol{j}_\alpha \cdot \boldsymbol{n}. \tag{A.3d}$$

where $\boldsymbol{u}$ is the displacement field, $\boldsymbol{f}$ is the volume-specific body force, r is the volume-specific rate of heat generation source, and $\boldsymbol{q}$ is the heat flux. Further, $\boldsymbol{i}_{\text{Max}} := \boldsymbol{h}\times\boldsymbol{\nabla}$ is the so-called Maxwell current, where $\boldsymbol{h}$ is the magnetizing field, $[\boldsymbol{h}]$ =A m^{-1} and $\boldsymbol{e}$ is the electric field. Moreover, μ_α is the chemical potential for any given species, $[\mu_\alpha]$ =J mol^{-1}. Introducing the identity $\boldsymbol{i} = \sum_\alpha z'_\alpha \boldsymbol{j}_\alpha$, transforming surface to volume integrals and using the appropriate balance equations, we obtain

$$\mathcal{P}_{\text{mech}} = \int_{\mathcal{B}} \boldsymbol{\sigma} : \partial_t \boldsymbol{\epsilon}\ \mathrm{d}V, \tag{A.4a}$$

$$\mathcal{P}_{\text{heat}} = \int_{\mathcal{B}} [r - \boldsymbol{q}\cdot\boldsymbol{\nabla}]\ \mathrm{d}V, \tag{A.4b}$$

$$\mathcal{P}_{\text{elec}} = \int_{\mathcal{B}} \boldsymbol{e}\cdot\partial_t\boldsymbol{d}\ \mathrm{d}V + \sum_\alpha \int_{\mathcal{B}} z'_\alpha \boldsymbol{j}_\alpha\cdot\boldsymbol{e}\ \mathrm{d}V \tag{A.4c}$$

$$\mathcal{P}_{\text{chem}} = \sum_\alpha \int_{\mathcal{B}} \left[\rho\partial_t c_\alpha \mu_\alpha - \boldsymbol{j}_\alpha\cdot\boldsymbol{\nabla}\mu_\alpha\right]\ \mathrm{d}V \tag{A.4d}$$

where $\boldsymbol{\epsilon}$ is the strain tensor. In order to derive (A.4a), we used the momentum balance (A.1a); to derive (A.4c), we used Ampere's law and the expression for the current density $\boldsymbol{i}$; while we used the continuity Eq. (A.1c) to derive (A.4d). We may thus localize (A.2) as

$$\partial_t e - \boldsymbol{\sigma} : \partial_t\boldsymbol{\epsilon} - \boldsymbol{e}\cdot\partial_t\boldsymbol{d} - \sum_\alpha \rho\mu_\alpha\partial_t c_\alpha + \boldsymbol{q}\cdot\boldsymbol{\nabla} + \sum_\alpha \boldsymbol{j}_\alpha\cdot\boldsymbol{\nabla}\mu'_\alpha = r, \tag{A.5}$$

where $\mu'_\alpha := \mu_\alpha + z'_\alpha\varphi$ is the chemical potential including the effect of the electric potential (often referred to as the electrochemical potential, cf. Newman and Thomas-Alyea (2004) and Salvadori et al. (2015)) associated with the α:th species.

A.3. Entropy inequality – constitutive equations

The standard global format of the entropy inequality reads

$$\int_{\mathcal{B}} \partial_t s\,\mathrm{d}V \geq \mathcal{R} \tag{A.6}$$

where s is the volume-specific internal entropy and $\mathcal{R}$ is the external entropy supply

$$\mathcal{R} := \int_{\mathcal{B}} \frac{r}{\theta}\,\mathrm{d}V - \int_{\partial\mathcal{B}} \frac{q_n}{\theta}\,\mathrm{d}S \tag{A.7}$$

In (A.7), θ is the absolute temperature. Eliminating the expression $r - \boldsymbol{q}\cdot\boldsymbol{\nabla}$ upon using the localized energy balance (A.5), we may obtain the localized form of (A.6) as follows:

$$-\partial_t e + \theta\partial_t s + \boldsymbol{\sigma} : \partial_t\boldsymbol{\epsilon} + \boldsymbol{e}\cdot\partial_t\boldsymbol{d} + \sum_\alpha \rho\mu_\alpha\partial_t c_\alpha - \frac{1}{\theta}\boldsymbol{q}\cdot\boldsymbol{\nabla}\theta - \sum_\alpha \boldsymbol{j}_\alpha\cdot\boldsymbol{\nabla}\mu'_\alpha \geq 0 \tag{A.8}$$

Separating terms conveniently, we may express this inequality as

$$\mathcal{D} = \mathcal{D}_{\text{ener}} + \mathcal{D}_{\text{heat}} + \mathcal{D}_{\text{elec}} + \mathcal{D}_{\text{el-chem}} \geq 0 \tag{A.9}$$

where the different terms are defined as

$$\mathcal{D}_{\text{ener}} = -\partial_t e + \theta\partial_t s + \boldsymbol{\sigma} : \partial_t\boldsymbol{\epsilon} + \boldsymbol{e}\cdot\partial_t\boldsymbol{d} + \sum_\alpha \rho\mu_\alpha\partial_t c_\alpha \tag{A.10a}$$

$$\mathcal{D}_{\text{heat}} = -\frac{1}{\theta}\boldsymbol{q}\cdot\boldsymbol{\nabla}\theta \tag{A.10b}$$

$$\mathcal{D}_{\text{el-chem}} = -\sum_\alpha \boldsymbol{j}_\alpha\cdot\boldsymbol{\nabla}\mu'_\alpha \tag{A.10c}$$

A stronger version of the entropy inequality is

- Clausius–Planck Inequality (CPI): $\mathcal{D}_{\text{ener}} \geq 0$
- Fourier Inequality (FI): $\mathcal{D}_{\text{heat}} \geq 0$
- Fick–Ohm Inequality[8]: $\mathcal{D}_{\text{el-chem}} \geq 0$

We shall consider these inequalities in turn:

[8] This nonstandard contribution is coined the Fick–Ohm Inequality for simplicity.

A.3.1. Clausisus-Planck inequality

We first note that the natural parametrization of e is $e(\boldsymbol{\epsilon}, s, \boldsymbol{d}, \underline{c})$,[9] where the components of $\underline{c}$ are the individual concentrations c_α. The next step is to introduce some kind of free energy by replacing s with θ via the appropriate Legendre transformation. We shall also replace $\boldsymbol{d}$ with $\boldsymbol{e}$. However, as to the role of $\underline{c}$ as the independent thermodynamic variable, the choice is less obvious. The two main possibilities (which both have advantages and disadvantages) are

- $\underline{c}$ is kept as the independent variable (which is the option chosen here)
- $\underline{c}$ is replaced by $\underline{\mu}$ as the independent variable

A volume-specific free energy density $\psi(\boldsymbol{\epsilon}, \theta, \boldsymbol{e}, \underline{c})$ is thus obtained via the double Legendre transformation

$$\psi(\boldsymbol{\epsilon}, \theta, \boldsymbol{e}, \underline{c}) = \min_{\hat{s}, \hat{\boldsymbol{d}}} \left[-\theta\hat{s} - \boldsymbol{e}\cdot\hat{\boldsymbol{d}} + e(\boldsymbol{\epsilon}, \hat{s}, \hat{\boldsymbol{d}}, \underline{c})\right] \tag{A.11}$$

Upon evaluating the min in (A.11), we obtain the corresponding stationarity conditions $\theta - \partial_s e = 0$, and $\boldsymbol{e} - \partial_{\boldsymbol{d}} e = \boldsymbol{0}$, from which it is assumed that it is possible to solve for $s, \boldsymbol{d}$ in terms of $\boldsymbol{\epsilon}, \theta, \boldsymbol{e}, \underline{c}$. Upon inserting into (A.10a), we obtain the equivalent inequality

$$\mathcal{D}_{\text{ener}} = -\partial_t\psi - s\partial_t\theta + \boldsymbol{\sigma} : \partial_t\boldsymbol{\epsilon} - \boldsymbol{d}\cdot\partial_t\boldsymbol{e} + \sum_\alpha \rho\mu_\alpha\partial_t c_\alpha \geq 0 \tag{A.12}$$

which can be rewritten as

$$\mathcal{D}_{\text{ener}} = \left[\boldsymbol{\sigma} - \partial_{\boldsymbol{\epsilon}}\psi\right] : \partial_t\boldsymbol{\epsilon} + \left[-s - \partial_\theta\psi\right]\partial_t\theta + \left[-\boldsymbol{d} - \partial_{\boldsymbol{e}}\psi\right]\cdot\partial_t\boldsymbol{e} + \sum_\alpha \left[\rho\mu_\alpha - \partial_{c_\alpha}\psi\right]\partial_t c_\alpha \geq 0 \tag{A.13}$$

We thus obtain the energetic constitutive relations

$$\boldsymbol{\sigma} = \partial_{\boldsymbol{\epsilon}}\psi,\ s = -\partial_\theta\psi,\ \boldsymbol{d} = -\partial_{\boldsymbol{e}}\psi,\ \mu_\alpha = \rho^{-1}\partial_{c_\alpha}\psi \tag{A.14}$$

A.3.2. Fourier inequality

It follows that $\mathcal{D}_{\text{heat}} \geq 0$, if the following (classical) sufficient condition is chosen:

$$\boldsymbol{q} = -\boldsymbol{K}\cdot\boldsymbol{\nabla}\theta \tag{A.15}$$

where $\boldsymbol{K}$ is the symmetric and positive (semi)definite thermal conductivity tensor, $[\boldsymbol{K}]$ = W m^{-1} K^{-1} that may represent anisotropy. In the simplest case $\boldsymbol{K}$ is state-independent.

A.3.3. Fick-Ohm inequality

It follows that $\mathcal{D}_{\text{el-chem}} \geq 0$ if the following sufficient condition is chosen:

$$\boldsymbol{j}_\alpha = -\boldsymbol{M}_\alpha\cdot\boldsymbol{\nabla}\mu'_\alpha = -\boldsymbol{M}_\alpha\cdot\boldsymbol{\nabla}\mu_\alpha + \boldsymbol{L}_\alpha\cdot\boldsymbol{e} = -\boldsymbol{M}_\alpha\cdot\boldsymbol{\nabla}\mu_\alpha - \boldsymbol{L}_\alpha\cdot\boldsymbol{\nabla}\varphi \tag{A.16}$$

where $\boldsymbol{M}_\alpha$ are symmetric and positive (semi)definite electrochemical mobility-diffusion tensors, $[\boldsymbol{M}_\alpha]$ = mol^2 m^{-1} s^{-1} J^{-1} that may represent anisotropy. In the simplest case $\boldsymbol{M}_\alpha$ is state-independent. Moreover, $\boldsymbol{L}_\alpha$ are defined as $\boldsymbol{L}_\alpha := z'_\alpha\boldsymbol{M}_\alpha$. The mass flux is thus composed of two physical mechanisms: Diffusion (driven by chemical potential gradients) and migration (driven by the electric field). As will be shown later, the chemical potential consists of a combination of concentration and (mean) stress.

A.4. The energy equation revisited

In standard fashion, we rephrase the energy balance in (A.5) in terms of the free energy density ψ (rather than the internal energy e) using the Legendre transformation (A.11). We then obtain the equation

$$\theta\partial_t s + \boldsymbol{q}\cdot\boldsymbol{\nabla} + \sum_\alpha \boldsymbol{j}_\alpha\cdot\boldsymbol{\nabla}\mu'_\alpha = r \tag{A.17}$$

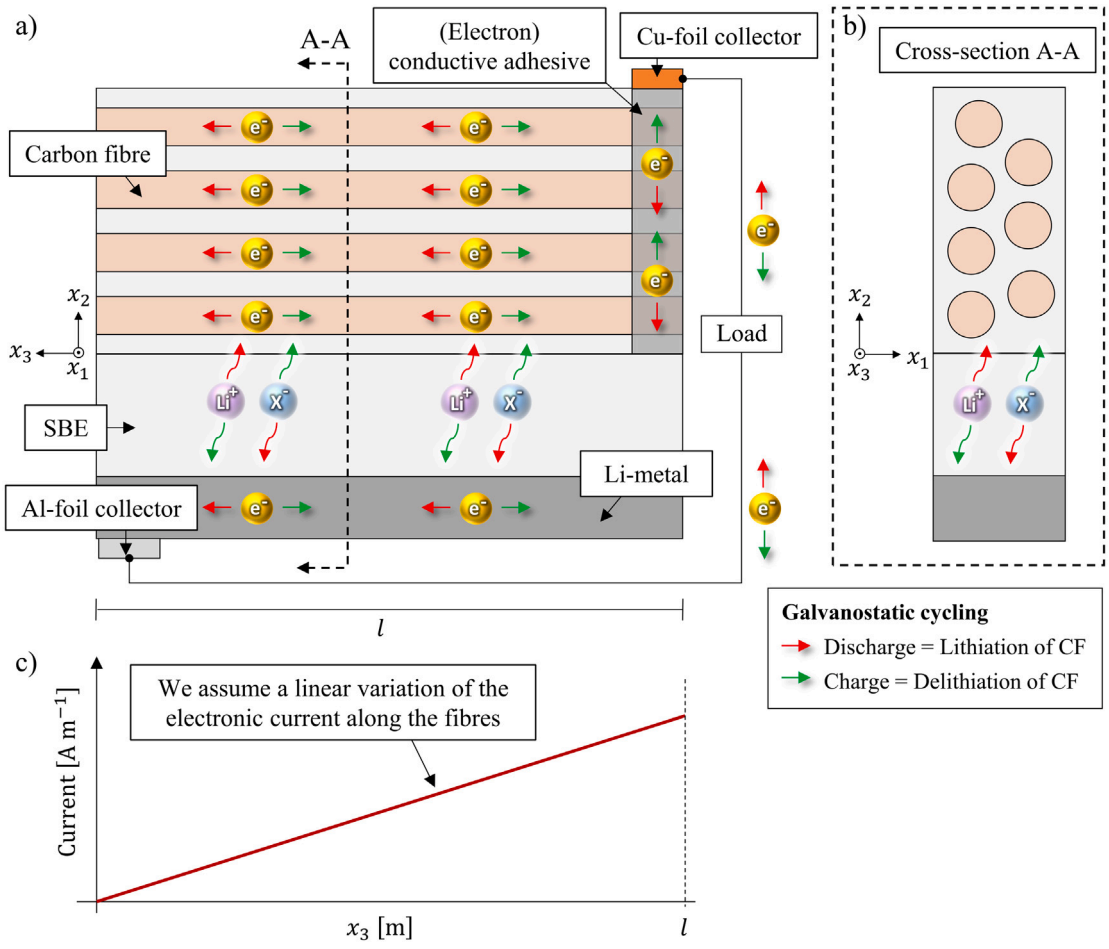

Fig. C.10. (a)–(b) Schematic illustration of the flow of charged species within the studied battery cell during operation. (c) Illustration of the assumed linear distribution of the electronic current along the fibre.

It is possible to expand $\partial_t s$ to obtain the linearized energy equation

$$\boldsymbol{\beta} : \partial_t \boldsymbol{\epsilon} + c_{\mathrm{v}} \partial_t \theta + \sum_{\alpha} \rho \gamma_{\alpha} \partial_t c_{\alpha} + \boldsymbol{\pi} \cdot \partial_t \boldsymbol{e} + \boldsymbol{q} \cdot \boldsymbol{\nabla} + \sum_{\alpha} \boldsymbol{j}_{\alpha} \cdot \boldsymbol{\nabla} \mu'_{\alpha} = r \tag{A.18}$$

where we introduced the quantities

$$\boldsymbol{\beta} := -\theta \partial^2_{\theta \boldsymbol{\epsilon}} \psi = -\theta \partial_{\theta} \boldsymbol{\sigma} \tag{A.19a}$$

$$c_{\mathrm{v}} := -\theta \partial^2_{\theta\theta} \psi = \theta \partial_{\theta} s \tag{A.19b}$$

$$\gamma_{\alpha} := -\rho^{-1} \theta \partial^2_{\theta c_{\alpha}} \psi = -\theta \partial_{\theta} \mu_{\alpha} \tag{A.19c}$$

$$\boldsymbol{\pi} := -\theta \partial^2_{\theta \boldsymbol{e}} \psi = \theta \partial_{\theta} \boldsymbol{d} \tag{A.19d}$$

Remark 5. If electronic current $\boldsymbol{i}_{\mathrm{e}^-}$ is accounted for, in addition to the ionic current, then (A.17) is generalized as

$$\theta \partial_t s + \boldsymbol{q} \cdot \boldsymbol{\nabla} + \sum_{\alpha} \boldsymbol{j}_{\alpha} \cdot \boldsymbol{\nabla} \mu'_{\alpha} - \boldsymbol{i}_{\mathrm{e}^-} \cdot \boldsymbol{e} = r \tag{A.20}$$

Upon introducing the identities $\mu'_{\alpha} = \mu_{\alpha} + z'_{\alpha} \varphi$ and $\boldsymbol{i} = \sum_{\alpha} z'_{\alpha} \boldsymbol{j}_{\alpha} + \boldsymbol{i}_{\mathrm{e}^-}$, we arrive at the alternative formulation

$$\theta \partial_t s + \boldsymbol{q} \cdot \boldsymbol{\nabla} + \sum_{\alpha} \boldsymbol{j}_{\alpha} \cdot \boldsymbol{\nabla} \mu_{\alpha} - \boldsymbol{i} \cdot \boldsymbol{e} = r \tag{A.21}$$

which is the generic format that holds whether electronic current is accounted for or not. □

[9] No dissipation is associated with deformation.

As to the further specification, we shall (in this paper) assume the following additive decomposition of the free energy density ψ:

$$\psi(\boldsymbol{\epsilon}, \theta, \boldsymbol{e}, \underline{c}) = \psi^{\text{me-th-ch}}(\boldsymbol{\epsilon}, \theta, \underline{c}) + \psi^{\text{el}}(\boldsymbol{e}) + \sum_{\alpha} \psi^{\text{ch}}_{\alpha}(\theta, c_{\alpha}) + \psi^{\text{th}}(\theta), \tag{A.22}$$

representing various couplings of mechanical, electrical, chemical and thermal contributions. These terms are defined explicitly in the main text. We note that, as a consequence of the specific parametrization (A.22), $\boldsymbol{\pi} = \boldsymbol{0}$.

Appendix B. Time-incremental weak format

The time-incremental weak format of the galvanostatic problem is derived as follows. First, the time intervals $I_n = (t_{n-1}, t_n)$, whose length is $\Delta t = t_n - t_{n-1}$, are introduced. Next we employ the Backward Euler method for time integration; however, we deviate from the fully implicit rule by replacing the constitutive mobility tensor $\boldsymbol{M}_{\alpha}({}^{n}c_{\alpha})$ by ${}^{n-1}\boldsymbol{M}_{\alpha} := \boldsymbol{M}_{\alpha}({}^{n-1}c_{\alpha})$ for $\alpha = \mathrm{Li,X}$, which infers forward differencing. Hence, we evaluate $\boldsymbol{j}_{\alpha} := {}^{n}\boldsymbol{j}_{\alpha}$ at $t = t_n$ as

$$\boldsymbol{j}_{\alpha}(\boldsymbol{\nabla}\mu_{\alpha}, \boldsymbol{\nabla}\varphi) = -{}^{n-1}\boldsymbol{M}_{\alpha} \cdot \boldsymbol{\nabla}\mu_{\alpha} - {}^{n-1}\boldsymbol{\mathcal{L}}_{\alpha} \cdot \boldsymbol{\nabla}\varphi, \ \alpha = \mathrm{Li,X} \tag{B.1}$$

where $\boldsymbol{\mathcal{L}}_{\mathrm{Li}} = F\boldsymbol{M}_{\mathrm{Li}}$ and $\boldsymbol{\mathcal{L}}_{\mathrm{X}} = -F\boldsymbol{M}_{\mathrm{X}}$.

The relevant solution (and test) spaces for solutions at the updated time t_n are defined as:

$$\hat{\mathbb{U}} = \hat{\mathbb{U}}^0 = \{\boldsymbol{u} \in \mathbb{H}^1(\Omega) : \ u_1 = 0 \text{ on } \Gamma_{\text{ext},2} \cup \Gamma_{\text{ext},3}\} \tag{B.2a}$$

$$\int_{\Omega_f \cup \Omega_e} \boldsymbol{\sigma} : \boldsymbol{\epsilon}[\delta \boldsymbol{u}] \, \mathrm{d}V = 0 \qquad \forall \delta \boldsymbol{u} \in \hat{\mathbb{U}}^0 \tag{B.3a}$$

$$\int_{\Omega_e} \rho^F F \left[c_{Li} - c_X\right] \delta\varphi \, \mathrm{d}V + \int_{\Omega_e} \boldsymbol{d} \cdot \boldsymbol{\nabla}[\delta\varphi] \, \mathrm{d}V - \int_{\Gamma_{fe} \cup \Gamma_+} d_n \delta\varphi \, \mathrm{d}S = 0 \qquad \forall \delta\varphi \in \hat{\mathbb{F}}^0 \tag{B.3b}$$

$$\begin{aligned} &\frac{1}{\Delta t} \int_{\Omega_f} \rho \left[c_{Li} - {}^{n-1}c_{Li}\right] \delta\mu_{Li} \, \mathrm{d}V + \frac{1}{\Delta t} \int_{\Omega_e} \rho^F \left[c_{Li} - {}^{n-1}c_{Li}\right] \delta\mu_{Li} \, \mathrm{d}V \\ &- \int_{\Omega_f \cup \Omega_e} \boldsymbol{j}_{Li} \cdot \boldsymbol{\nabla}[\delta\mu_{Li}] \, \mathrm{d}V - \int_{\Gamma_{fe}} j_{Li,n} [\![\delta\mu_{Li}]\!] \, \mathrm{d}S + \int_{\Gamma_+} j_{Li,n} \delta\mu_{Li} \, \mathrm{d}S = 0 \end{aligned} \qquad \forall \delta\mu_{Li} \in \hat{\mathbb{M}}^0_{Li} \tag{B.3c}$$

$$\frac{1}{\Delta t} \int_{\Omega_e} \rho^F \left[c_X - {}^{n-1}c_X\right] \delta\mu_X \, \mathrm{d}V - \int_{\Omega_e} \boldsymbol{j}_X \cdot \boldsymbol{\nabla}[\delta\mu_X] \, \mathrm{d}V = 0 \qquad \forall \delta\mu_X \in \hat{\mathbb{M}}^0_X \tag{B.3d}$$

$$\int_{\Omega_f \cup \Omega_e} \left[\mu^{en}_{Li} - \mu_{Li}\right] \delta c_{Li} \, \mathrm{d}V = 0 \qquad \forall \delta c_{Li} \in \mathbb{L}_2(\Omega_f \cup \Omega_e) \tag{B.3e}$$

$$\int_{\Omega_e} \left[\mu^{en}_X - \mu_X\right] \delta c_X \, \mathrm{d}V = 0 \qquad \forall \delta c_X \in \mathbb{L}_2(\Omega_e) \tag{B.3f}$$

$$\begin{aligned} &\frac{1}{\Delta t} \int_{\Omega_e \cup \Omega_f} C_v \left[\theta - {}^{n-1}\theta\right] \delta\theta \, \mathrm{d}V - \int_{\Omega_e \cup \Omega_f} \boldsymbol{q} \cdot \boldsymbol{\nabla}[\delta\theta] \, \mathrm{d}V \\ &+ \int_{\Omega_e} [\boldsymbol{j}_X \cdot \boldsymbol{\nabla}\mu_X] \delta\theta \, \mathrm{d}V + \int_{\Omega_f \cup \Omega_e} [\boldsymbol{j}_{Li} \cdot \boldsymbol{\nabla}\mu_{Li}] \delta\theta \, \mathrm{d}V \\ &+ \int_{\Omega_e} \left[F[\boldsymbol{j}_{Li} - \boldsymbol{j}_X] \cdot \boldsymbol{\nabla}\varphi\right] \delta\theta \, \mathrm{d}V + \int_{\Gamma_{ext,1}} q_n \delta\theta \, \mathrm{d}S - \int_{\Gamma_{fe}} \bar{q}_n [\![\delta\theta]\!] \, \mathrm{d}S \\ &+ \int_{\Gamma_{fe}} \Delta q_n \frac{1}{2} \left[\delta\theta^e + \delta\theta^f\right] \mathrm{d}S = \int_{\Omega_f} Q_{elec} \delta\theta \, \mathrm{d}V \end{aligned} \qquad \forall \delta\theta \in \hat{\mathbb{T}}^0 \tag{B.3g}$$

$$\delta\Phi^- \left[\int_{\Gamma_{fe}} i_n \, \mathrm{d}S - I^-\right] = 0 \qquad \forall \delta\Phi^- \in \mathbb{R} \tag{B.3h}$$

Box I.

$$\hat{\mathbb{F}} = \hat{\mathbb{F}}^0 = \{\varphi \in \mathbb{H}^1(\Omega_e)\} \tag{B.2b}$$

$$\hat{\mathbb{M}}_{Li} = \hat{\mathbb{M}}^0_{Li} = \{\mu_{Li} \in \mathbb{L}_2(\Omega_f \cup \Omega_e),\ \mu_{Li}|_{\Omega_f} = \mathbb{H}^1(\Omega_f),\ \mu_{Li}|_{\Omega_e} = \mathbb{H}^1(\Omega_e)\} \tag{B.2c}$$

$$\hat{\mathbb{M}}_X = \hat{\mathbb{M}}^0_X = \{\mu_X \in \mathbb{H}^1(\Omega_e)\} \tag{B.2d}$$

$$\hat{\mathbb{T}} = \hat{\mathbb{T}}^0 = \{\theta \in \mathbb{H}^1(\Omega)\} \tag{B.2e}$$

For the galvanostatic problem, the potential value $\Phi^+(t)$ is prescribed along the boundary Γ_+, whereas the total current $I^-(t)$ from/to the negative collector (fibre) domains $\Omega_f := \cup_i \Omega_{f,i}$ is assumed to be a known function. The entire problem of solving for the updated fields at $t = t_n$ can now be posed as follows: Find $\boldsymbol{u} \in \hat{\mathbb{U}}$, $\varphi \in \hat{\mathbb{F}}$, $\mu_{Li} \in \hat{\mathbb{M}}_{Li}$, $\mu_X \in \hat{\mathbb{M}}_X$, $c_{Li} \in \mathbb{L}_2(\Omega_f \cup \Omega_e)$, $c_X \in \mathbb{L}_2(\Omega_e)$, $\theta \in \hat{\mathbb{T}}$, and $\Phi^- \in \mathbb{R}$, that solve the set of equations (B.3a)–(B.3h) given in Box I, where the pertinent constitutive relations are presented in Sections Section 3.1.2 (Ω_f), Section 3.2.2 (Ω_e), Section 3.3 (Γ_{fe}) and Section 3.4 ($\Gamma_{ext} \cup \Gamma_+$).

Appendix C. Flow of charged species during electro-chemical cycling

The flow of charged species within the studied battery cell during operation is schematically illustrated in Figs. C.10a–b. Further, we assume a linear distribution of the electronic current along the fibres as illustrated in Fig. C.10c.

Appendix D. Symbols and parameters

Symbols and parameters used in the analysis presented in this paper are listed in Tables D.1 and D.2, respectively.

D.1. FE-approximations

The polynomial order of the triangular Lagrange elements used for the various primary fields in the fibres and the SBE domains are as follows: $\boldsymbol{u}$ cubic (fibre, SBE), φ quadratic (SBE), μ_{Li} quadratic (fibre, SBE), μ_X quadratic (SBE), c_{Li} quadratic (fibre, SBE), c_X quadratic (SBE),

Table D.1
List of symbols.

Symbol	Unit	Description
φ	[V]	Electrical potential
μ_α	[J mol^{-1}]	Chemical potential of species α = Li,X
c_α	[mol kg^{-1}]	Ion concentration of species α = Li,X = molar bulk density of ions divided by bulk density
$\tilde{c}_\alpha$	[–]	Normalized ion concentration of species α = Li,X
$\boldsymbol{\sigma}$	[Pa]	Stress tensor
$\mathbf{E}$	[Pa]	Elasticity tensor
$\boldsymbol{u}$	[m]	Displacement field tensor

(continued on next page)

Table D.1 (*continued*).

Symbol	Unit	Description
$\boldsymbol{\epsilon}$	[−]	Strain tensor
$\boldsymbol{\epsilon}^{\mathrm{ch}}$	[−]	Insertion strain
$\boldsymbol{\alpha}^{\mathrm{ch}}$	[kg mol^{-1}]	Insertion tensor
$\boldsymbol{\epsilon}^{\mathrm{th}}$	[−]	Thermal strain
$\boldsymbol{\alpha}^{\mathrm{th}}$	[K^{-1}]	Thermal expansion tensor
$\boldsymbol{j}_{\alpha}$	[mol m^{-2} s^{-1}]	Total ion flux vector of species α = Li,X
η_{α}	[m^{2}mol s^{-1} J^{-1}]	Mobility coefficient of species α = Li,X
$\boldsymbol{M}_{\alpha}$	[mol^2 m^{-1} s^{-1} J^{-1}]	Mobility tensor for species α = Li,X
$\boldsymbol{K}$	[W m^{-1} K^{-1}]	Thermal conductivity tensor
$\boldsymbol{q}$	[W m^{-2}]	Heat flux
$\boldsymbol{\mathcal{K}}$	[S m^{-1}]	Ionic conductivity ($\boldsymbol{\mathcal{K}} = F^2[\boldsymbol{M}_{\mathrm{Li}} + \boldsymbol{M}_{\mathrm{X}}]$)
$\boldsymbol{\mathcal{E}}$	[F m^{-1}]	Permittivity tensor
$\bar{M}$	[mol^2 m^{-2} s^{-1} J^{-1}]	Interface mobility
$\bar{\boldsymbol{\mathcal{K}}}$	[S m^{-2}]	Interface ionic conductivity ($\bar{\boldsymbol{\mathcal{K}}} = F^2\bar{M}$)
$\bar{\mathcal{E}}$	[F m^{-2}]	Interface permittivity
$\boldsymbol{i}$	[A m^{-2}]	Current density
$\boldsymbol{d}$	[C m^{-2}]	Electric flux density vector
θ	[K]	Temperature
ε	[F m^{-1}]	Permittivity
L	[Pa]	Lamé's first parameter
G	[Pa]	Shear modulus
$H_{\parallel}$	[Pa]	Uniaxial strain modulus
Φ^{+}	[V]	Positive electrode potential (set to 0)
Φ^{-}	[V]	Negative electrode (fibre) potential
I^{-}	[A m^{-1}]	Total applied/prescribed current per unit length
$\boldsymbol{\sigma}_n$	[Pa]	Traction
δ	[m]	Thickness of electric double layer
t	[s]	Time
Ω	[−]	Domain
Γ	[−]	Boundary
ρ	[kg m^{-3}]	Density of carbon fibre
ρ^{F}	[kg m^{-3}]	Intrinsic density of fluid (electrolyte) in SBE
ϕ	[−]	Porosity of SBE
C_{v}	[J m^{-3} K^{-1}]	Volume specific heat capacity
$\bar{K}^{\mathrm{th}}$	[W m^{-2} K^{-1}]	Interface heat transfer coefficient
κ^{f}	[S m^{-1}]	Electronic conductivity of the fibre
i^{f}	[A m^{-2}]	Applied current density
$i^{\mathrm{f}}_{\mathrm{m}}$	[A kg^{-1}]	Applied mass-specific current defined per kg of fibres
A^{f}	[m^2]	The total cross-sectional area of fibres
l	[m]	Fibre length
Q_{elec}	[W m^{-3}]	Generated heat due to the electric current in the fibres

Table D.2
Material parameter values.

Parameter	Value	Unit	Description	Reference
$H_{\parallel}$	296	[GPa]	Uniaxial strain modulus fibre	Duan et al. (2020)
$L_{\parallel}$	5.5	[GPa]	Lamé's first parameter parallel fibre	Duan et al. (2020)
$L^0_{\perp}$	4.7	[GPa]	Lamé's first parameter perpendicular fibre ($\tilde{c}_{\mathrm{Li}} = 0$)	Duan et al. (2020, 2021)
$G_{\parallel}$	12.5	[GPa]	Shear modulus parallel (i.e. $x_3 - x_{1/2}$ plane) fibre	Duan et al. (2020)
$G_{\perp}$	9.4	[GPa]	Shear modulus perpendicular (i.e. $x_1 - x_2$ plane) fibre	Duan et al. (2020)
L	0.47	[GPa]	Lamé's first parameter SBE	Carlstedt et al. (2022b) and Ihrner et al. (2017)
G	0.08	[GPa]	Shear modulus SBE	Carlstedt et al. (2022b) and Ihrner et al. (2017)
$\eta^{\mathrm{e}}_{\mathrm{Li}}$	$3.24 \cdot 10^{-15}$	[m^2 mol s^{-1} J^{-1}]	Mobility of Li^+ in SBE ($\tilde{c}_{\mathrm{Li}} = 1$)	Carlstedt et al. (2022b) and Ihrner et al. (2017)
$\eta^{\mathrm{e}}_{\mathrm{X}}$	$3.24 \cdot 10^{-15}$	[m^2 mol s^{-1} J^{-1}]	Mobility of X^- in SBE ($\tilde{c}_{\mathrm{X}} = 1$)	Carlstedt et al. (2022b) and Ihrner et al. (2017)
η_{Li}	$5.8 \cdot 10^{-18}$	[m^2 mol s^{-1} J^{-1}]	Mobility of Li in fibre (based on diffusion coefficient)	Kjell et al. (2013)
$\alpha^{\mathrm{ch}}_{\perp}$	$1.60 \cdot 10^{-3}$	[kg mol^{-1}]	Transverse insertion expansion coefficient	Jacques et al. (2013a)
$\alpha^{\mathrm{ch}}_{\parallel}$	$3.19 \cdot 10^{-4}$	[kg mol^{-1}]	Longitudinal insertion expansion coefficient	Jacques et al. (2013a)
$\alpha^{\mathrm{th}}_{\perp}$	$1 \cdot 10^{-5}$	[K^{-1}]	Transverse thermal expansion coefficient fibre	Bowles and Tompkins (1989)

(*continued on next page*)

Table D.2 (*continued*).

Parameter	Value	Unit	Description	Reference
$\alpha_{\parallel}^{\text{th}}$	$-0.54 \cdot 10^{-6}$	[K^{-1}]	Longitudinal thermal expansion coefficient fibre	Bowles and Tompkins (1989)
α^{th}	$2 \cdot 10^{-5}$	[K^{-1}]	Thermal expansion coefficient SBE	Bowles and Tompkins (1989)
$c_{\text{Li,ini}}$	$6.27 \cdot 10^{-2}$	[mol kg^{-1}]	Initial Li-concentration in fibre	–
$c_{\text{Li,max}}$	6.27	[mol kg^{-1}]	Maximum Li-concentration in fibre	Jacques et al. (2013a)
$c_{\alpha,\text{ref}}/c_{\alpha,0}$	1	[mol kg^{-1}]	Reference/initial concentration of Li^+ and X^- in the SBE	Ihrner et al. (2017) and Schneider et al. (2019)
$c_{\alpha,\text{sat}}$	3	[mol kg^{-1}]	Saturation (max) concentration of Li^+ and X^- in the (electrolyte) SBE	Nyman et al. (2008)
ε_0	$8.854 \cdot 10^{-12}$	[F m^{-1}]	Vacuum permittivity	–
ε_r	10	[–]	Relative permittivity	Fontanella and Wintersgill (1988) and Ganser et al. (2019)
i_0	1	[A m^{-2}]	Exchange current density	Kjell et al. (2013)
μ_{Li}^0	$4.98 \cdot 10^4$	[J mol^{-1}]	Reference chemical potential Li in fibre (vs. Li/Li^+), at $\tilde{c}_{\text{Li},0}$	Kjell et al. (2013)
μ_{α}^0	0	[J mol^{-1}]	Reference chemical potential Li^+ and X^- in SBE	–
ρ	1850	[kg m^{-3}]	Fibre density	–
ρ^{F}	1000	[kg m^{-3}]	Intrinsic density of fluid (electrolyte) in SBE	–
δ	$0.5 \cdot 10^{-9}$	[m]	Thickness of electric double layer	Ganser et al. (2019) and Braun et al. (2015)
F	96485	[C mol^{-1}]	Faraday's constant	–
R	8.314	[J K^{-1} mol^{-1}]	Gas constant	–
$k_{\parallel}$	11.3	[W m^{-1} K^{-1}]	Longitudinal thermal conductivity fibre	Torayca (2018)
$k_{\perp}$	1.3	[W m^{-1} K^{-1}]	Transverse thermal conductivity fibre	Torayca (2018) and Zantout and Zhupanska (2010)
k	0.175	[W m^{-1} K^{-1}]	Thermal conductivity SBE	Zantout and Zhupanska (2010)
$\theta_0/\theta_{\text{ext}}$	293.15	[K]	Initial and external temperature	–
κ^{f}	$6.9 \cdot 10^4$	[S m^{-1}]	Electronic conductivity of the fibre	Kjell et al. (2013)
$\tilde{\mathcal{K}}^{\text{th}}$	$5.3 \cdot 10^5$	[W m^{-2} K^{-1}]	Fibre-SBE interface heat transfer coefficient	Macedo and Ferreira (2003)
C_{v}	$1.37 \cdot 10^6$	[J m^{-3} K^{-1}]	Volume specific heat capacity fibre	Torayca (2018)
C_{v}^{e}	$10^5 - 10^7$	[J m^{-3} K^{-1}]	Volume specific heat capacity SBE (baseline value = $2 \cdot 10^6$)	Zantout and Zhupanska (2010)
$\tilde{\mathcal{K}}_{\text{ext}}^{\text{th}}$	$1 - 10$	[W m^{-2} K^{-1}]	Heat exchange coefficient (baseline value = 1)	Gigliotti et al. (2011) and Xu et al. (2022)
l	$0.1 - 0.2$	[m]	Fibre length (baseline value = 0.1)	Johannisson et al. (2018)

θ quadratic (fibre, SBE). The selected polynomial orders (for a given triangulation) are based on a convergence study, which shows that the results are reliable and not flawed by discretization errors.

References

Al Hallaj, S., Maleki, H., Hong, J.S., Selman, J.R., 1999. Thermal modeling and design considerations of lithium-ion batteries. J. Power Sources 83, 1–8. http://dx.doi.org/10.1016/S0378-7753(99)00178-0.

Armand, M., Axmann, P., Bresser, D., Copley, M., Edström, K., Ekberg, C., Guyomard, D., Lestriez, B., Novák, P., Petranikova, M., Porcher, W., Trabesinger, S., Wohlfahrt-Mehrens, M., Zhang, H., 2020. Lithium-ion batteries – Current state of the art and anticipated developments. J. Power Sources 479, 228708. http://dx.doi.org/10.1016/j.jpowsour.2020.228708.

Asp, L.E., Bouton, K., Carlstedt, D., Duan, S., Harnden, R., Johannisson, W., Johansen, M., Johansson, M., Lindbergh, G., Liu, F., Peuvot, K., Schneider, L.M., Xu, J., Zenkert, D., 2021. A structural battery and its multifunctional performance. Adv. Energy Sustain. Res 2, 2000093. http://dx.doi.org/10.1002/aesr.202000093.

Asp, L.E., Johansson, M., Lindbergh, G., Xu, J., Zenkert, D., 2019. Structural battery composites: a review. Funct. Compos. Struct. 1, 042001. http://dx.doi.org/10.1088/2631-6331/ab5571.

Bowles, D.E., Tompkins, S.S., 1989. Prediction of coefficients of thermal expansion for unidirectional composites. J. Compos. Mater. 23, 370–388. http://dx.doi.org/10.1177/002199838902300405.

Braun, S., Yada, C., Latz, A., 2015. Thermodynamically consistent model for space-charge-layer formation in a solid electrolyte. J. Phys. Chem. C 119, 22281–22288. http://dx.doi.org/10.1021/acs.jpcc.5b02679.

Cano, Z.P., Banham, D., Ye, S., Hintennach, A., Lu, J., Fowler, M., Chen, Z., 2018. Batteries and fuel cells for emerging electric vehicle markets. Nat. Energy 3, 279–289. http://dx.doi.org/10.1038/s41560-018-0108-1.

Carlstedt, D., Asp, L.E., 2019. Thermal and diffusion induced stresses in a structural battery under galvanostatic cycling. Compos. Sci. Technol. 179, 69–78. http://dx.doi.org/10.1016/j.compscitech.2019.04.024.

Carlstedt, D., Asp, L.E., 2020. Performance analysis framework for structural battery composites in electric vehicles. Composites B 186, 107822. http://dx.doi.org/10.1016/j.compositesb.2020.107822.

Carlstedt, D., Marklund, E., Asp, L.E., 2019. Effects of state of charge on elastic properties of 3D structural battery composites. Compos. Sci. Technol. 169, 26–33. http://dx.doi.org/10.1016/j.compscitech.2018.10.033.

Carlstedt, D., Rittweger, F., Runesson, K., Navarro-Suárez, A.M., Xu, J., Duan, S., Larsson, F., Riemschneider, K.-R., Asp, L.E., 2022a. Experimental and computational characterization of carbon fibre based structural battery electrode laminae. Compos. Sci. Technol. 220, 109283. http://dx.doi.org/10.1016/j.compscitech.2022.109283.

Carlstedt, D., Runesson, K., Larsson, F., Vinh, T., Jänicke, R., Asp, L.E., 2022b. Computational modelling of structural batteries accounting for stress-assisted convection in the electrolyte. Int. J. Solids Struct. 238, 111343. http://dx.doi.org/10.1016/j.ijsolstr.2021.111343.

Carlstedt, D., Runesson, K., Larsson, F., Xu, J., Asp, L.E., 2020. Electro-chemo-mechanically coupled computational modelling of structural batteries. Multifunct. Mater. 3, 045002. http://dx.doi.org/10.1088/2399-7532/abc60d.

Doyle, M., Fuller, T.F., Newman, J., 1993. Modeling of galvanostatic charge and discharge of the lithium/polymer/insertion cell. J. Electrochem. Soc. 140, 1526. http://dx.doi.org/10.1149/1.2221597.

Duan, S., Iyer, A.H.S., Carlstedt, D., Rittweger, F., Sharits, A., Maddox, C., Riemschneider, K.R., Mollenhauer, D., Colliander, M., Liu, F., Asp, L.E., 2021. Effect of lithiation on the elastic moduli of carbon fibres. Carbon 185, 234–241. http://dx.doi.org/10.1016/j.carbon.2021.09.037.

Duan, X., Jiang, W., Zou, Y., Lei, W., Ma, Z., 2018. A coupled electrochemical–thermal–mechanical model for spiral-wound li-ion batteries. J. Mater. Sci. 53, 10987–11001. http://dx.doi.org/10.1007/s10853-018-2365-6.

Duan, S., Liu, F., Pettersson, T., Creighton, C., Asp, L.E., 2020. Determination of transverse and shear moduli of single carbon fibres. Carbon 158, 772–782. http://dx.doi.org/10.1016/j.carbon.2019.11.054.

Federico, D., Salgado, R.M., Oliveira, J.E., Arteiro, A., Camanho, P.P., Braga, M.H., 2021. Structural batteries: A review. Molecules 26, http://dx.doi.org/10.3390/molecules26082203.

Fontanella, J.J., Wintersgill, M.C., 1988. Low frequency dielectric properties of polyether electrolytes. In: Polymer Electrolyte Reviews, Vol. 2.

Forgez, C., Vinh, D.D., Friedrich, G., Morcrette, M., Delacourt, C., 2010. Thermal modeling of a cylindrical LiFePO4/graphite lithium-ion battery. J. Power Sources 195, 2961–2968. http://dx.doi.org/10.1016/j.jpowsour.2009.10.105.

Ganser, M., Hildebrand, F.E., Kamlah, M., McMeeking, R.M., 2019. A finite strain electro-chemo-mechanical theory for ion transport with application to binary solid electrolytes r. J. Mech. Phys. Solids 125, 681–713. http://dx.doi.org/10.1016/j.jmps.2019.01.004.

Gigliotti, M., Lafarie-Frenot, M.C., C., G.J., 2011. Development of experimental and modelling tools for the characterisation of the thermo-electro-mechanical behaviour of composite materials for aircraft applications. Méc. Ind. 12, 7–101. http://dx.doi.org/10.1051/meca/2011012.

Goudarzi, M., Grazioli, D., Simone, A., 2022. An efficient computational approach for three-dimensional modeling and simulation of fibrous battery electrodes. Internat. J. Numer. Methods Engrg. 123, 1513–1546. http://dx.doi.org/10.1002/nme.6881.

Hagberg, J., Maples, H., Alvim, K., Xu, J., Johannisson, W., Bismarck, A., Zenkert, D., Lindbergh, G., 2018. Lithium iron phosphate coated carbon fiber electrodes for structural lithium ion batteries. Compos. Sci. Technol. 162, 235–243. http://dx.doi.org/10.1016/j.compscitech.2018.04.041.

Harnden, R., Carlstedt, D., Zenkert, D., Lindbergh, G., 2022. Multifunctional carbon fibre composite: a structural, energy harvesting, strain-sensing material. Submitted for Publication.

Hong, Z., Hu, Z., Yang, R., You, J., Fu, Y., Zhou, L., Yin, S., 2021. Multiphysics modeling framework for composite structural batteries with modified carbon fibers as electrodes. Compos. Commun. 27, 100853. http://dx.doi.org/10.1016/j.coco.2021.100853.

Hu, B., Ma, Z., Lei, W., Zou, Y., Lu, C., 2017. A chemo-mechanical model coupled with thermal effect on the hollow core–shell electrodes in lithium-ion batteries. Theor. Appl. Mech. Lett. 7, 199–206. http://dx.doi.org/10.1016/j.taml.2017.09.001.

Ihrner, N., Johannisson, W., Sieland, F., Zenkert, D., Johansson, M., 2017. Structural lithium ion battery electrolytes: Via reaction induced phase-separation. J. Mater. Chem. A 5, 25652–25659. http://dx.doi.org/10.1039/C7TA04684G.

Jacques, E., Hellqvist Kjell, M., Zenkert, D., Lindbergh, G., Behm, M., 2013a. Expansion of carbon fibres induced by lithium intercalation for structural electrode applications. Carbon 59, 246–254. http://dx.doi.org/10.1016/j.carbon.2013.03.015.

Jacques, E., Kjell, M.H., Zenkert, D., Lindbergh, G., 2013b. Piezo-electrochemical effect in lithium-intercalated carbon fibres. Electrochem. Commun. 35, 65–67. http://dx.doi.org/10.1016/j.elecom.2013.07.040.

Johannisson, W., Harnden, R., Zenkert, D., Lindbergh, G., 2020. Shape-morphing carbon fiber composite using electrochemical actuation. Proc. Natl. Acad. Sci. 117 (14), 7658–7664. http://dx.doi.org/10.1073/pnas.1921132117.

Johannisson, W., Ihrner, N., Zenkert, D., Johansson, M., Carlstedt, D., Asp, L.E., Sieland, F., 2018. Multifunctional performance of a carbon fiber UD lamina electrode for structural batteries. Compos. Sci. Technol. 168, 81–87. http://dx.doi.org/10.1016/j.compscitech.2018.08.044.

Kaessmair, S., Runesson, K., Steinmann, P., Jänicke, R., Larsson, F., 2021. Variationally consistent computational homogenization of chemomechanical problems with stabilized weakly periodic boundary conditions. Internat. J. Numer. Methods Engrg. 122 (22), 6429–6454. http://dx.doi.org/10.1002/nme.6798.

Kjell, M.H., Zavalis, T.G., Behm, M., Lindbergh, G., 2013. Electrochemical characterization of lithium intercalation processes of PAN-based carbon fibers in a microelectrode system. J. Electrochem. Soc. 160, A1473–A1481. http://dx.doi.org/10.1149/2.054309jes.

Ladpli, P., Nardari, R., Kopsaftopoulos, F., Chang, F.K., 2019. Multifunctional energy storage composite structures with embedded lithium-ion batteries. J. Power Sources 414, 517–529. http://dx.doi.org/10.1016/j.jpowsour.2018.12.051.

Lutkenhaus, J.L., Flouda, P., 2020. Structural batteries take a load off. Science Robotics 5, http://dx.doi.org/10.1126/scirobotics.abd7026.

Macedo, F., Ferreira, J.A., 2003. Thermal contact resistance evaluation in polymer-based carbon fiber composites. Rev. Sci. Instrum. 74, 828–830. http://dx.doi.org/10.1063/1.1520325.

Moyer, K., Meng, C., Marshall, B., Assal, O., Eaves, J., Perez, D., Karkkainen, R., Roberson, L., Pinta, C.L., 2020. Carbon fiber reinforced structural lithium-ion battery composite: Multifunctional power integration for CubeSats. Energy Storage Mater. 24, 676–681. http://dx.doi.org/10.1016/j.ensm.2019.08.003.

Newman, J., Thomas-Alyea, K.E., 2004. Electrochemical Systems. In: The ECS Series of Texts and Monographs, Wiley.

Newman, J., Tiedemann, W., 1975. Porous electrode theory with battery applications. AIChE J. 21, 25–41. http://dx.doi.org/10.1002/aic.690210103.

Nyman, A., Behm, M., Lindbergh, G., 2008. Electrochemical characterisation and modelling of the mass transport phenomena in LiPF6–EC–EMC electrolyte. Electrochim. Acta 53, 6356–6365. http://dx.doi.org/10.1016/j.electacta.2008.04.023.

Pejman, R., Kumbur, E.C., Najafi, A.R., 2021. Multi-physics design optimization of structural battery. Multifunct. Mater. 4, 024001. http://dx.doi.org/10.1088/2399-7532/abf158.

Rezaei, S., Asheri, A., Xu, B.-X., 2021. A consistent framework for chemo-mechanical cohesive fracture and its application in solid-state batteries. J. Mech. Phys. Solids 157, 104612. http://dx.doi.org/10.1016/j.jmps.2021.104612.

Salvadori, A., Grazioli, D., Geers, M.G.D., 2015. Governing equations for a two-scale analysis of Li-ion battery cells. Int. J. Solids Struct. 59, 90–109. http://dx.doi.org/10.1016/j.ijsolstr.2015.01.014.

Salvadori, A., McMeeking, R., Grazioli, D., Magri, M., 2018. A coupled model of transport-reaction-mechanics with trapping. Part I – Small strain analysis. J. Mech. Phys. Solids 114, 1–30. http://dx.doi.org/10.1016/j.jmps.2018.02.006.

Sanchez, J.S., Xu, J., Xia, Z., Sun, J., Asp, L.E., Palermo, V., 2021. Electrophoretic coating of LiFePO4/Graphene oxide on carbon fibers as cathode electrodes for structural lithium ion batteries. Compos. Sci. Technol. 208, 108768. http://dx.doi.org/10.1016/j.compscitech.2021.108768.

Schäfer, A.W., Barrett, S.R.H., Doyme, K., Dray, L.M., Gnadt, A.R., Self, R., O'Sullivan, A., Synodinos, A.P., Torija, A.J., 2019. Technological, economic and environmental prospects of all-electric aircraft. Nat. Energy 4, 160–166. http://dx.doi.org/10.1038/s41560-018-0294-x.

Schneider, L.M., Ihrner, N., Zenkert, D., Johansson, M., 2019. Bicontinuous electrolytes via thermally initiated polymerization for structural lithium ion batteries. ACS Appl. Energy Mater. 2, 4362–4369. http://dx.doi.org/10.1021/acsaem.9b00563.

Schutzeichel, M.O.H., Kletschkowski, T., Linde, P., Asp, L.E., 2019. Experimental characterization of multifunctional polymer electrolyte coated carbon fibres. Funct. Compos. Struct. 1, 025001. http://dx.doi.org/10.1088/2631-6331/ab136b.

Schutzeichel, M.O.H., Kletschkowski, T., Monner, H.P., 2021. Microscale thermal modelling of multifunctional composite materials made from polymer electrolyte coated carbon fibres including homogenization and model reduction strategies. Appl. Mech. 2, 739–765. http://dx.doi.org/10.3390/applmech2040043.

Singh, A., Pal, S., 2020. Coupled chemo-mechanical modeling of fracture in polycrystalline cathode for lithium-ion battery. Int. J. Plast. 127, 102636. http://dx.doi.org/10.1016/j.ijplas.2019.11.015.

Thomas, K.E., Newman, J., 2003. Thermal modeling of porous insertion electrodes. J. Electrochem. Soc. 150, A176. http://dx.doi.org/10.1149/1.1531194.

2018. Torayca. In: T800S Data Sheet. URL: https://www.toraycma.com/wp-content/uploads/T800S-Technical-Data-Sheet-1.pdf.pdf.

Tu, V., Asp, L.E., Shirsova, N., Larsson, F., Runesson, K., Jänicke, R., 2020. Performance of bicontinuous structural electrolytes. Multifunct. Mater. 3, 025001. http://dx.doi.org/10.1088/2399-7532/ab8d9b.

Wang, M., Emre, A., Tung, S., Gerber, A., Wang, D., Huang, Y., Cecen, V., Kotov, N.A., 2019. Biomimetic solid-state Zn2+ electrolyte for corrugated structural batteries. ACS Nano 13, 1107–1115. http://dx.doi.org/10.1021/acsnano.8b05068.

Wang, Y., Wu, H., Sun, L., Jiang, W., Lu, C., Ma, Z., 2021. Coupled electrochemical-mechanical modeling with strain gradient plasticity for lithium-ion battery electrodes. Eur. J. Mech. A Solids 87, 104230. http://dx.doi.org/10.1016/j.euromechsol.2021.104230.

Xu, J., Geng, Z., Johansen, M., Carlstedt, D., Duan, S., Thiringer, T., Liu, F., Asp, L.E., 2022. A multicell structural battery composite laminate. EcoMat e12180. http://dx.doi.org/10.1002/eom2.12180.

Xu, J., Lindbergh, G., Varna, J., 2018a. Carbon fiber composites with battery function: Stresses and dimensional changes due to li-ion diffusion. J. Compos. Mater. 52, 2729–2742. http://dx.doi.org/10.1177/0021998317752825.

Xu, J., Lindbergh, G., Varna, J., 2018b. Multiphysics modeling of mechanical and electrochemical phenomena in structural composites for energy storage: Single carbon fiber micro-battery. J. Reinf. Plast. Compos. 37, 701–715. http://dx.doi.org/10.1177/0731684418760207.

Yin, S., Hong, Z., Hu, Z., Liu, B., Gao, X., Li, Y., Xu, J., 2020. Fabrication and multiphysics modeling of modified carbon fiber as structural anodes for lithium-ion batteries. J. Power Sources 476, 228532. http://dx.doi.org/10.1016/j.jpowsour.2020.228532.

Zantout, A.E., Zhupanska, O.I., 2010. On the electrical resistance of carbon fiber polymer matrix composites. Composites A 41, 1719–1727. http://dx.doi.org/10.1016/j.compositesa.2010.08.010.

Zhang, X., Chumakov, S., Li, X., Klinsmann, M., Kim, S.U., Linder, C., Christensen, J., 2020. An electro-chemo-thermo-mechanical coupled three-dimensional computational framework for lithium-ion batteries. J. Electrochem. Soc. 167, 160542. http://dx.doi.org/10.1149/1945-7111/abd1f2.